

# THE CORES OF THE Fe K $\alpha$ LINES IN ACTIVE GALACTIC NUCLEI: AN EXTENDED Chandra HIGH ENERGY GRATING SAMPLE

X. W. Shu<sup>1,2</sup>, T. Yaqoob<sup>2</sup>, J. X. Wang<sup>1</sup>

## ABSTRACT

We extend the study of the core of the Fe K $\alpha$  emission line at  $\sim 6.4$  keV in Seyfert galaxies reported in Yaqoob & Padmanabhan (2004) using a larger sample observed by the *Chandra* High Energy Grating (HEG). The sample consists of 82 observations of 36 unique sources with  $z < 0.3$ . Whilst heavily obscured active galactic nuclei (AGNs) are excluded from the sample, these data offer some of the highest precision measurements of the peak energy of the Fe K $\alpha$  line, and the highest spectral resolution measurements of the width of the core of the line in unobscured and moderately obscured ( $N_H < 10^{23}$  cm $^{-2}$ ) Seyfert galaxies to date. From an empirical and uniform analysis, we present measurements of the Fe K $\alpha$  line centroid energy, flux, equivalent width (EW), and intrinsic width (FWHM). The Fe K $\alpha$  line is detected in 33 sources, and its centroid energy is constrained in 32 sources. In 27 sources the statistical quality of the data is good enough to yield measurements of the FWHM. We find that the distribution in the line centroid energy is strongly peaked around the value for neutral Fe, with over 80% of the observations giving values in the range 6.38–6.43 keV. Including statistical errors, 30 out of 32 sources ( $\sim 94\%$ ) have a line centroid energy in the range 6.35–6.47 keV. The mean equivalent width, amongst the observations in which a non-zero lower limit could be measured, was  $53 \pm 3$  eV. The mean FWHM from the subsample of 27 sources was  $2060 \pm 230$  km s $^{-1}$ . The mean EW and FWHM are somewhat higher when multiple observations for a given source are averaged. From a comparison with the H $\beta$  optical emission-line widths (or, for one source, Br $\alpha$ ), we find that there is no universal location of the Fe K $\alpha$  line-emitting region relative to the optical BLR. In general, a given source may have contributions to the Fe K $\alpha$  line flux from parsec-scale distances from the putative black hole,

---

<sup>1</sup> CAS Key Laboratory for Research in Galaxies and Cosmology, Department of Astronomy, University of Science and Technology of China, Hefei, Anhui 230026, P. R. China, xwshu@mail.ustc.edu.cn

<sup>2</sup>Department of Physics and Astronomy, Johns Hopkins University, Baltimore, MD 21218, yaqoob@skysrv.pha.jhu.edu

down to matter a factor  $\sim 2$  closer to the black hole than the BLR. We confirm the presence of the X-ray Baldwin effect, an anti-correlation between the Fe  $K\alpha$  line EW and X-ray continuum luminosity. The HEG data have enabled isolation of this effect to the narrow core of the Fe  $K\alpha$  line.

*Subject headings:* galaxies: active – line: profile – X-rays: galaxies

## 1. INTRODUCTION

The narrow core (FWHM  $< 10,000$  km s $^{-1}$ ) of the Fe  $K\alpha$  fluorescent emission, peaking at  $\sim 6.4$  keV is a common and dominant feature of the X-ray spectrum of active galactic nuclei (AGNs) that have a 2–10 keV X-ray luminosity less than  $\sim 10^{45}$  erg s $^{-1}$  (e.g. Sulentic et al. 1998; Lubiński & Zdziarski 2001; Weaver, Gelbord, & Yaqoob 2001; Perola et al. 2002; Yaqoob & Padmanabhan 2004 (hereafter YP04); Levenson et al. 2006; Winter et al. 2009). The luminosity in the core of the Fe  $K\alpha$  emission may be comparable to any additional, relativistically-broadened Fe  $K\alpha$  line emission that may be present, and indeed, in many cases may be the *only* component of the Fe  $K\alpha$  line (e.g. see Guainazzi, Bianchi, & Dovčiak 2006; Nandra et al. 2007; Miller 2007; Turner & Miller 2009; Bianchi et al. 2009). Measurement of the properties of the core of the Fe  $K\alpha$  line in AGN is important for two principal reasons. One is to constrain the physical properties of the large-scale structure in the central engine. The peak energy of the Fe  $K\alpha$  line constrains the ionization state of the line-emitting matter, and the width of the line gives kinematic information that can be used to estimate the size and location of the X-ray reprocessor. The equivalent width (EW) of the Fe  $K\alpha$  line is a function of geometry, column density, covering factor, element abundances, and orientation of the line-emitter. Another reason why spectroscopy of the Fe  $K\alpha$  line core is important is that it is necessary to model the narrow component of the line in order to deconvolve any relativistically-broadened emission-line component that may be present. The *Chandra* high energy grating (HEG; see Markert et al. 1995) is still unsurpassed in spectral resolution in the Fe K band, which at 6.4 keV is  $\sim 39$  eV, or  $\sim 1860$  km s $^{-1}$  FWHM. This is a factor of  $\sim 4$  better than the spectral resolution of X-ray CCD detectors aboard *XMM-Newton* and *Suzaku*. Although broad Fe  $K\alpha$  emission lines are better studied with CCD spectrometers (due to their higher throughput), the *Chandra* HEG is well-suited for studying the narrow core of the Fe  $K\alpha$  line. One can then utilize the HEG measurements to deconvolve narrow and broad Fe  $K\alpha$  line components in lower spectral resolution data.

In YP04 the results of a uniform analysis of the properties of the Fe  $K\alpha$  emission-line core were presented, based on *Chandra* HEG data of a modest sample of fifteen AGN. There are now a larger number of *Chandra* HEG observations for which the data are available, and

in the present paper we extend the study of YP04 to include 82 observations of 36 unique AGN. The paper is organized as follows. In §2 we describe the observations and data. In §3 we describe the methodology and basic spectral-fitting results. In §4 we discuss the implications of the results for the properties of the core of narrow Fe K $\alpha$  emission line in the HEG AGN sample. In §5 we investigate whether the narrow core of the Fe K $\alpha$  line as isolated by the HEG, supports the so-called X-ray Baldwin effect (an anti-correlation between the line EW and X-ray luminosity and between the EW and a proxy for the accretion rate). In §6 we summarize our results and findings.

## 2. OBSERVATIONS AND DATA

The *Chandra HETGS* (*High Energy Transmission Grating Spectrometer*) consists of two grating assemblies, a High-Energy Grating (HEG) and a Medium-Energy Grating (MEG), and it is the HEG that achieves the highest spectral resolution. The MEG has only half of the spectral resolution of the HEG and less effective area in the Fe K band, so our study will focus on the HEG data. Our study is based on data from *Chandra HETGS* AGN observations that were public as of 2008, September 30, filtering on several criteria. Firstly, we selected non-blazar AGN that had  $z < 0.3$ . This actually only omitted one source, PKS 2149–306 ( $z = 2.345$ ), which is a high-luminosity radio-loud quasar (see Fang et al. 2001 for results from the *Chandra* grating observations). Since the centroid energy of the Fe K $\alpha$  line appears at  $\sim 6.4/(1+z)$  keV, the line would appear at very different places on the instrumental effective area curve for very different values of  $z$ . In addition, the EW of the Fe K $\alpha$  line is smaller by a factor  $(1+z)$  compared to the rest-frame value. Therefore, a restriction on the sample redshift also helps to achieve a more homogeneous analysis. Next we required that the total counts in the full HEG bandpass ( $\sim 0.9 - 8$  keV) was  $> 1500$ , a condition which rejects spectra that have insufficient signal-to-noise ratios for our purpose. Relaxing this criterion would only have admitted two sources, PG 1404+226, and 1H 0707–495. We then selected those AGN that are known to have X-ray absorbing column densities less than  $10^{23}$  cm $^{-2}$ . The reason for this is that AGN with higher column densities have X-ray spectra that are complex and measurements of the properties of even the narrow Fe K $\alpha$  line core in such sources can become model-dependent. Indeed, Murphy & Yaqoob (2009; hereafter MY09) showed, using monte carlo simulations of X-ray reprocessing, that inclination-angle and geometrical effects on the EW of the Fe K $\alpha$  line become important for column densities greater than  $\sim 10^{23}$  cm $^{-2}$ . Although the column density out of the line-of-sight could be larger than the line-of-sight column density, it is the simplicity of the observed spectrum that is the driver of the selection. We will present a study of heavily-absorbed AGN observed by the *Chandra* HEG elsewhere. Our approach in the present paper is to perform a very simple

*empirical* analysis in order to obtain robust measurements of the basic narrow Fe K $\alpha$  line core parameters that are not dependent on details of how the continuum is modeled. Our selection criteria then populate our sample with some sources that are formally classified as type 2 AGN, whereas the study of YP04 included strictly only type 1 AGN.

We also excluded 15 *Chandra HETGS* observations of M81 ( $\sim 435$  ks exposure) from the study, as its very low luminosity and accretion rate set it apart from the rest of the bright AGN in the sample (it is most often classified as a LINER harboring a low-luminosity AGN). The bolometric luminosity of M81 is only  $\sim 10^{-5}$  of the Eddington luminosity (Young et al. 2007). We note that the results of some *HETGS* results for M81, based on  $\sim 280$  ks exposure time have been presented by Young et al. (2007) who found K-shell emission lines from He-like and H-like Fe in addition to the Fe K $\alpha$  line at  $\sim 6.4$  keV. Our final sample consists of 82 observations of 36 unique AGN and includes all of the observations in YP04 (which we re-analyzed for the present paper). We note that our sample includes 3C 273, which is sometimes classified as a blazar. However, this source is variable and often shows Seyfert-like properties (e.g. Grandi & Palumbo 2007).

The *Chandra* data for the sample were reduced and HEG spectra were made as described in Yaqoob et al. (2003) and YP04. We used only the first orders of the grating data (combining the positive and negative arms). The mean HEG count rates ranged from  $0.026 \pm 0.001$  ct/s for the weakest source (PDS 456) to  $1.161 \pm 0.006$  for the brightest source (IC 4329a). The exposure time ranged from  $\sim 20$  ks to  $\sim 172$  ks per observation, but was  $\sim 50 - 120$  ks for most of the sources. Nineteen sources were observed more than once, and the largest net exposure time from summed data from observations of the same source was  $\sim 880$  ks (NGC 3783). The observations, identified by target name, sequence number, and observation ID (“ObsID”), are listed in Table 1, along with the net exposure times for the spectra. Further details of all of the observations can be found in the *Chandra* data archive at <http://cda.harvard.edu/chaser/>. Higher-level products, including lightcurves and spectra for each observation can be found in the databases *HotGAS* (<http://hotgas.pha.jhu.edu>), and *TGCat* (<http://tgcate.mit.edu/>). Background was not subtracted since it is negligible over the energy range of interest (e.g. see Yaqoob et al. 2003). Note that the systematic uncertainty in the HEG wavelength scale is  $\sim 433$  km s $^{-1}$  ( $\sim 11$  eV) at 6.4 keV <sup>1</sup>.

---

<sup>1</sup><http://space.mit.edu/CXC/calib/hetgcal.html>

### 3. SPECTRAL FITTING METHODOLOGY AND RESULTS

The spectra were analyzed using the spectral-fitting package XSPEC (Arnaud 1996). Since we are interested in utilizing the highest possible spectral resolution available, we used spectra binned at  $0.0025\text{\AA}$ , and this amply oversamples the HEG resolution ( $0.012\text{\AA}$  FWHM). The  $C$ -statistic was used for minimization. All model parameters will be referred to the source frame. Our method is simply to fit a simple continuum plus Gaussian emission-line model over the 2–7 keV band for each spectrum. Above 7 keV the HEG effective area rapidly decreases. We found, as in YP04, that if the energy band is restricted any further the constraints on the Fe  $K\alpha$  line parameters do not improve because when the intrinsic line width is free there is degeneracy of the line parameters with the continuum slope. In most cases a simple power-law continuum was adequate, but for some sources an additional uniform, neutral, absorber component was included (namely NGC 2110, MCG -5-23-16, NGC 4151 and NGC 5506). In no case was a column density greater than  $4.3_{-0.3}^{+0.4} \times 10^{22} \text{ cm}^{-2}$  required. Galactic absorption was not included for any of the sources because such small column densities have little effect above 2 keV. Thus, there were a maximum of six free parameters in the model, namely the power-law slope and its overall normalization,  $\Gamma$ , the column density,  $N_H$ , the centroid energy of the Gaussian emission-line component,  $E_0$ , its flux,  $I_{\text{Fe K}}$ , and its width,  $\sigma_{\text{Fe K}}$ . The approach of using an over-simplified continuum model is necessitated by the limited bandpass of the HEG data ( $\sim 2 - 7$  keV) but since we are interested in the narrow core of the Fe  $K\alpha$  emission line, at the spectral resolution of the HEG, this is not restrictive. Obviously, use of such an empirical model means that we should not assign a physical meaning to  $\Gamma$  and  $N_H$ .

The signal-to-noise ratio of the spectra showed a wide range so we followed a systematic, two-step procedure that accounts for this. In the first round of analysis we fixed the emission-line width,  $\sigma_{\text{Fe K}}$ , at 1 eV (corresponding to  $\sim 110 \text{ km s}^{-1}$  FWHM at 6.4 keV), a value well below the instrument resolution, because the line width could not be constrained in all the data sets. Uniformly freezing the line width for all the data sets then picks up the narrowest, unresolved core component of the emission line for all the data sets. In the second round of analysis we allowed the line width to float. Where multiple observations of a given source were available we constructed and fitted spectra that were averaged over all of the observations, in addition to fitting data from the individual observations. Inter-observation variability will be discussed in §4.4.

The results of this first round of analysis are shown in Table 1 which shows the derived equivalent width (EW) in addition to the other Fe  $K\alpha$  line parameters. Note that since the models were fitted by first folding through the instrument response before comparing with the data, the derived line parameters *do not* need to be corrected for instrumental response.

We do not give the best-fitting values of  $\Gamma$  or  $N_H$  in Table 1 because the values derived using the simplistic continuum model are not physically meaningful but are simply parameterizations. The 2–10 keV continuum fluxes and luminosities shown in Table 1 were obtained by extrapolating the best-fitting model up to 10 keV. We caution that such extrapolation could give inaccurate fluxes and luminosities if the continuum shape is significantly different in the 7–10 keV band compared to the extrapolated model. The fluxes are not corrected for absorption, but the luminosities are. The  $\Delta C$  values shown in Table 1 correspond to the decrease in  $C$  when the narrow, two-parameter emission line was added to the continuum-only model, and is therefore a measure of the significance of the emission line.

We found that in some cases (fourteen observations of ten sources, plus the summed spectrum of IRAS 18325 – 5926) the Fe  $K\alpha$  line centroid energy could not be constrained, and in such cases the centroid energy was fixed at 6.40 keV. In twelve of these data sets the Fe  $K\alpha$  line was not detected at a confidence level greater than 90% and for these cases only an upper limit on the EW, and line flux,  $I_{\text{Fe K}}$ , could be obtained. Two sets of statistical errors are given for the Fe  $K\alpha$  line parameters in Table 1 for each spectral fit. The first set corresponds to 68% confidence ( $\Delta C = 2.279$ , or 0.989, depending on whether there were two parameters or one parameter free respectively in the Gaussian component). These “1- $\sigma$ ” errors are useful for performing standard statistical analyses on the model parameters. However, as a more conservative measure, the 90% confidence *range* (for the appropriate number of free parameters of the Gaussian component) for each line parameter is also given in Table 1 (values in parentheses). For the 90% confidence ranges  $\Delta C = 4.605$  and 2.706 for two parameters and one parameter free respectively.

We also found that in some sources that have multiple observations, the Fe  $K\alpha$  line parameters were sometimes better constrained from some of the individual observations than from the averaged spectra because the latter may contain contributions from data in which the Fe  $K\alpha$  line was relatively weaker in EW. Detailed interpretation of the results in Table 1 will be given in §4.

In the second round of spectral fitting we allowed the intrinsic width of the Gaussian emission-line component to be a free parameter. However, in situations when the signal-to-noise ratio of the Fe  $K\alpha$  emission line is too poor, the Gaussian model emission-line component can become very broad as it then begins to model the continuum, resulting in values of the width that are not actually related to the physical width of the emission line. As a very loose initial criterion, we rejected all cases in which a three-parameter Gaussian component was detected with less than 95% confidence (corresponding to rejecting fits that gave  $\Delta C < 7.8$ ). This rough criterion immediately rejected fits for which the fits actually became unstable and left 26 unique sources and 65 data sets, including 14 spectra averaged

over multiple observations. The results for all of the fits with  $\Delta C > 7.8$  are shown in Table 2, in which the three-parameter, 68% statistical errors and 90% confidence ranges on the line parameters are given. The Fe K $\alpha$  line width is given as a FWHM in km s $^{-1}$  rather than the Gaussian width,  $\sigma_{\text{Fe K}}$ .

The next selection criterion we used was more specifically focussed on determining whether the model width was a measure of the true line width. Owing to the excellent spectral resolution of the HEG it is straightforward to determine when the model FWHM is no longer a measure of the Fe K $\alpha$  emission-line width by reconciling the spectral data with the confidence contours of  $I_{\text{FeK}\alpha}$  versus the centroid energy,  $E_{\text{FeK}\alpha}$ . This can be seen in Fig. 1 and Fig. 2 which show, for a given source, the rest-frame spectra in the Fe K region alongside the confidence contours of  $I_{\text{FeK}\alpha}$  versus  $E_{\text{FeK}\alpha}$ . We have not shown plots for all the data sets (spectra for all of the data sets can be found in the databases mentioned in §1). For example, we have not shown plots for data sets that have already been presented in YP04. Nor have we shown plots for data sets in which the detection of the Fe K $\alpha$  line was marginal or insignificant. Fig. 1 shows results for sources that have only one observation whilst Fig. 2 shows time-averaged spectra for sources with multiple observations, alongside confidence contours for the individual and time-averaged data. We see in Fig. 1 and Fig. 2 that in some cases the 99% confidence contours indicate a range in centroid energy that is clearly much larger than the breadth of the emission-line feature that can be estimated directly from the spectral plots. For example, for NGC 985 the joint, two-parameter, 99% confidence contour of line intensity versus center energy (solid line) is  $\sim 600$  eV wide. However, from the spectral plot in the Fe K band, the Fe K $\alpha$  line clearly has a width less than  $\sim 250$  eV. Thus the 99% confidence bounds on line flux versus line centroid energy imply that the Gaussian component is in fact modeling the continuum, resulting in very large FWHM values that are not actually related to the physical width of the emission line. For this case of NGC 985, we constructed a 99% confidence contour (dotted line in Fig. 1) of the line intensity versus energy with the Gaussian width fixed at 1 eV (110 km s $^{-1}$ ). This shows that the centroid energy is constrained to be in the range  $\sim 6.3 - 6.5$  keV, consistent with the physical width of the narrow core in the spectral plot.

Thus, by comparing the line intensity versus line energy confidence contours with the spectra we determined that the FWHM constraints deduced from spectral fits for 16 out of the 65 data sets were not reliable indicators of the Fe K $\alpha$  line core intrinsic width (none of the 16 are data sets summed over multiple observations). We found that the situations in which the Gaussian width model parameter became an unreliable indicator of the emission-line intrinsic width generally corresponded to a 90% confidence, two-parameter upper limit on the FWHM greater than  $\sim 15,000$  km s $^{-1}$ . We note that even for the cases where we can obtain a reliable measure of the Fe K $\alpha$  line FWHM, the true line width may be less than

the FWHM deduced from our simplistic model-fitting because there may be blending from an unresolved Compton-shoulder component and/or from several (low) ionization states of Fe. Also, the difference in rest energy of  $\sim 13$  eV of the individual components of the Fe  $K\alpha$  line ( $K\alpha_1$  and  $K\alpha_2$ ) may increase the apparent FWHM if the line is modeled with a single Gaussian model component. However, the separation of  $K\alpha_1$  and  $K\alpha_2$  corresponds to  $\sim 600$  km s $^{-1}$  (three times less than the HEG resolution in the Fe K band), and considering the  $K\alpha_1:K\alpha_2$  branching ratio of 2:1, Yaqoob et al. (2001) showed that artificial broadening is not a concern for line parameters and signal-to-noise ratio that are typical of the HEG observations reported here.

In the present paper we are concerned only with the Fe  $K\alpha$  line core centered at  $\sim 6.4$  keV, and not emission lines from highly ionized species of Fe. Nevertheless, overlaid on the spectra in Fig. 1 are vertical dashed lines marking the positions of the Fe xxv He-like triplet lines (the two intercombination lines are shown separately), Fe xxvi Ly $\alpha$ , Fe I  $K\beta$ , and the Fe K-shell threshold absorption-edge energy. The values adopted for these energies were from NIST<sup>2</sup> (He-like triplet); Pike et al. 1996 (Fe xxvi Ly $\alpha$ ); Palmeri et al. 2003 (Fe I  $K\beta$ ), and Verner et al. 1996 (Fe K edge). Emission lines *and* absorption lines from highly ionized species of Fe have indeed been reported in the literature for some of the same data sets discussed in the present paper (e.g. see Bianchi et al. 2005). We summarize such results from the literature in the appendix for each source as appropriate, including any previous results on the 6.4 keV emission line that are based on the same data that we have employed. We also give in the appendix any unusual details and/or issues for particular data sets that are pertinent to our analysis of the *HETGS* data.

#### 4. PROPERTIES OF THE CORE OF THE FE $K\alpha$ LINE EMISSION

Table 3 summarizes various mean quantities from the Fe  $K\alpha$  line measurements, calculated in two different ways. In the first method we used the measurements from individual observations and in the second method we used measurements that are representative of properties *per source*. For the latter, in most cases this utilized measurements from spectra averaged over multiple observations where relevant, except for NGC 526, PG 0834, 3C 273, IRAS 13349+2438 and 3C 382. For these five sources the Fe  $K\alpha$  line was significantly detected in only one observation and combining observations led to looser constraints on the Fe  $K\alpha$  line parameters, as previously explained in §3. Thus we used only the one observation for these five sources that showed the best detection of the Fe  $K\alpha$  line. This may bias the

---

<sup>2</sup><http://physics.nist.gov/PhysRefData>



results because we do not know if non-detections of the Fe  $K\alpha$  are due to variability. We caution that any sample properties derived using our results should take account of such possible biases. We also caution that the *Chandra* grating sample is subject to very peculiar and unquantifiable selection effects because of the restrictions on the kind of sources that are suitable for observations with gratings (or more precisely, which sources proposal review panels judge to be suitable for observations with gratings). Thus, the *Chandra* grating AGN archive is not suitable for unbiased population studies. The principal purpose of the present work is to systematically quantify the spectral parameters from the data.

#### 4.1. LINE CENTROID ENERGY

From our analysis, we were able to measure the Fe  $K\alpha$  line centroid energy in 32 out of 36 unique sources for at least one spectrum (see Table 1 and Table 2). Table 3 summarizes four different weighted mean line centroid energies. One pair of measurements was derived from individual observations and the other pair was derived from *per source* measurements (as described above). Each mean centroid energy was derived from spectral-fitting results in which the intrinsic line width was fixed (Table 1), and from results in which the intrinsic line width was not fixed in all the spectra (Table 2). Here, and hereafter, for the calculation of the weighted mean of any quantity with asymmetric errors, we simply assumed symmetric errors, using the largest 68% confidence error from spectral fitting. For the line centroid values, 68 out of 82 spectra contributed to the “per observation” means, and 32 sources contributed to the “per source” means. It can be seen from Table 3 that all four mean line centroid energies are within  $-12$  eV and  $+3$  eV of 6.400 keV (including statistical bounds).

Note that the statistical errors on the mean centroid energies are 1 eV or better but they may be biased by the brightest sources and largest exposure times. A more useful measure of the dispersion in the line energies may be gleaned from examining the distribution of energies. Fig. 3 shows histograms of the Fe  $K\alpha$  line centroid energy. Again, we show four histograms: Fig. 3(a) and Fig. 3(c) pertain to “per observation” results and Fig. 3(b) and Fig. 3(d) pertain to “per source” results. Fig. 3(a) and Fig. 3(b) pertain to Fe  $K\alpha$  line centroid energies measured with the intrinsic line width fixed (Table 1), and Fig. 3(c) and Fig. 3(d) pertain to results obtained when the intrinsic line width was not fixed in all the observations (Table 2). The dashed and dotted lines correspond to histograms made from the 68% confidence lower and upper limits on the line centroid energy respectively. The fits in which the Fe  $K\alpha$  line width was fixed gave line centroid energies that are more reliable indicators of the peak line energy because the fits with the line width free are more prone to the centroid energy being affected by the shape of the line profile. All panels show

that the histograms are not Gaussian but sharply peaked at  $\sim 6.4$  keV. There is not a significant difference between the “per observation” and “per source” distributions, within the statistical errors. For the “per observation” fits with the Fe  $K\alpha$  line width fixed, we found that  $\sim 80\%$  of the best-fitting line centroid energies lie in the range 6.38–6.43 keV, a spread of only 50 eV. Another way of expressing our results is that if we take the highest signal-to-noise measurement for each source (i.e. utilizing results from the summed spectra only, for sources with multiple observations), we find that 21 out of 32 sources ( $\sim 66\%$ ) have 68% confidence statistical bounds on the line centroid energy that lie entirely in the range 6.38–6.43 keV. A similar procedure also shows that 30 out of 32 sources ( $\sim 94\%$ ) have 68% confidence bounds on the line centroid energy that lie entirely in the range 6.35–6.47 keV. We note that we might have expected to observe additional peaks in the centroid energy distribution blueward of 6.4 keV due to highly ionized Fe. Although such emission lines have been detected in HEG data (e.g. NGC 7314, Yaqoob et al. 2003; NGC 7213, Bianchi et al. 2008), the HEG effective area is already very small at 6.4 keV (only  $\sim 20$  cm<sup>-2</sup>) and drops very rapidly at higher energies. Higher throughput detectors such as those aboard *XMM-Newton* or *Suzaku* are more suitable for investigating the frequency of occurrence of highly ionized Fe emission lines.

We now examine those measurements that deviate significantly from the 6.4 keV peak of the Fe  $K\alpha$  line centroid energy distribution in Fig. 3. For 3C 273 and 4C 74.26, we obtained Fe  $K\alpha$  line centroid energies lower than those for the bulk of the measurements, and we note that even the 90% confidence upper limits were less than 6.4 keV for the fits in which the line width was fixed (see Table 1). For the fits in which the line width was free, the corresponding upper limits were 6.49 keV and 6.39 keV for 3C 273 and 4C 74.26 respectively (see Table 2). However, for these two sources, the detection of the Fe  $K\alpha$  line was marginal:  $C$  decreased by less than 9.3 when a narrow Gaussian was added to a power-law continuum-only model. Thus, the lines were detected with only 99% confidence or less. Such low centroid energies are not unphysical. For example they could be affected by gravitational redshifts. We note that a weak broad Fe  $K\alpha$  line has been detected in 3C 273 by *XMM – Newton* (Page et al. 2004a) and the 99% confidence contour does not rule a line with a centroid energy in the range  $\sim 6.2$ -6.3 keV. Interestingly, a narrow component of the Fe  $K\alpha$  line at 6.2 keV, in addition to an Fe  $K\alpha$  line at  $\sim 6.4$  keV, has been detected in 4C 74.26 by *XMM – Newton* (Ballantyne & Fabian 2005).

For PG 0844+346, we obtained a centroid energy for the Fe  $K\alpha$  line consistent with 6.4 keV from the fits with the line width fixed (see Table 1). However, allowing the line width to float gave a centroid energy of  $\sim 6.6$  keV, with a 90% confidence lower limit of 6.42 keV (see Table 2). The reason for this apparently discrepant behavior is clear from the spectrum of PG 0844+346 in Fig. 1. The spectrum shows an emission line centered at

$\sim 6.4$  keV and this is picked up in the fits for which the line width was fixed (the measured energy was  $6.364_{-0.009}^{+0.007}$  keV). The spectrum also shows two additional peaks at higher energies, albeit with a low signal-to-noise ratio. Allowing the single-line Gaussian model width to be free in the fits then causes the line component to model all three narrow lines by broadening the Gaussian.

In summary, we measured the centroid energy of the Fe  $K\alpha$  emission line in 32 out of 36 sources. In 30 out of the 32 sources the line centroid energy lies in the range 6.35–6.47 keV, inclusive of the 68% confidence statistical errors. We note that ionization states less than Fe XVII correspond to Fe  $K\alpha$  line energies less than 6.43 keV (e.g. Palmeri et al. 2003; Mendoza et al. 2004). When individual sources amongst the 30 are considered, the line centroid energy can constrain the ionization state to be much lower than Fe XVII in some cases. In the remaining 2 sources, 3C 273 and 4C 74.26, the line centroid energy, including statistical errors, appears to be lower than 6.4 keV, but the detection is marginal in these two sources.

## 4.2. LINE EQUIVALENT WIDTH

From the spectral-fitting results for which the Fe  $K\alpha$  line intrinsic width was fixed (Table 1), 33 of the 36 sources have at least one spectrum from which we could measure the EW with a non-zero 90% confidence lower limit and a finite upper limit. The three sources for which only upper limits on the EW could be obtained were Mkn 705, PDS 456, and IRAS 18325–5926. In total, 70 out of 82 of the individual observations in Table 1 yielded bounded lower and upper limits on the EW. We calculated weighted mean EW values in four different ways (as we did for the line centroid energy in §4.1): i.e. from “per observation” and “per source” values, each set obtained with the intrinsic line width fixed in all spectral fits (Table 1) and with the intrinsic line width free in some of the spectra (Table 2). The resulting mean EW values are summarized in Table 3. It can be seen that the mean Fe  $K\alpha$  EW is somewhat sensitive to how it is calculated, ranging from 42 eV to 70 eV, with a statistical error of 4 eV or less. We note, however that a value of  $\sim 40$  eV could be interpreted as a fairly robust sample lower limit on the EW of any unresolved core of the Fe  $K\alpha$  line.

Fig. 4 shows histograms of the Fe  $K\alpha$  line EW, again constructed in four different ways. Fig. 4(a) and Fig. 4(c) pertain to “per observation” results and Fig. 4(b) and Fig. 4(d) pertain to “per source” results. Fig. 4(a) and Fig. 4(b) pertain to Fe  $K\alpha$  line EWs measured with the intrinsic line width fixed (Table 1), and Fig. 4(c) and Fig. 4(d) pertain to results obtained when the intrinsic line width was not fixed in all the observations (Table 2).

The dashed and dotted histograms in Fig. 4 correspond to the distributions of the 68% confidence lower and upper limits on EW, respectively. The shaded histograms in both panels are the 68% upper limits on the EW for the 12 observations in which the EW could not be measured. For the “per observation” and intrinsic line width fixed results, Table 1 and Fig. 4(a) show that the maximum best-fitting EW of the Fe K $\alpha$  line core is 162 eV, and >90% of the measurements have a best-fitting EW less than 100 eV. We also found that 79% of the measurements have a 68% confidence upper limit on the EW of less than 100 eV (23 unique sources). Including the results from the fits with the Fe K $\alpha$  line width free, we found that  $\sim 70\%$  of the “per observation” measurements have a best-fitting equivalent EW less than 100 eV (Fig. 4(c)). Within the statistical errors, the histograms obtained from the “per observation” results are not significantly different to the corresponding “per source” histograms. Note that in Fig. 4(c) and Fig. 4(d), we do not show the measurement for PG 0844+346, as its EW is artificially high ( $\sim 600$  eV) because it is not a true measure of the EW of the emission line at  $\sim 6.4$  keV (see §3).

From a theoretical point of view, the Fe K $\alpha$  line EW depends on a number of factors, including geometry, orientation, column density, and covering factor of the line-emitting matter distribution, as well as element abundances. Time delays between variations in the continuum level and the Fe K $\alpha$  line flux also affect the EW measured during a given observation. The sample EW results should therefore be interpreted in terms of a particular geometry. The relatively small dispersion of the EW distribution that we measure from the HEG data translates into a small dispersion in the parameters mentioned above, but it is difficult to uniquely constrain these parameters from the EW distribution due to degeneracy. In the context of the toroidal X-ray reprocessor model of MY09, which subtends a solid angle of  $2\pi$  at the X-ray source, the measured EW distribution is consistent with the MY09 model if the mean of the EW distribution corresponds to column densities greater than  $\sim 2 \times 10^{23}$  cm $^{-2}$  (see MY09). This column density does not refer to the line-of-sight value, but rather to the angle-average over all incident X-ray continuum radiation. Comparison of the HEG results with the toroidal reprocessor models of Ghisellini, Haardt, & Matt (1994) and Ikeda, Awaki, & Terashima (2009) leads to similar conclusions. The upper bound on the column density is not constrained because, for situations in which the Fe K $\alpha$  line is observed for lines of sight that intercept a column density  $< 10^{23}$  cm $^{-2}$ , the EW attains a maximum for an angle-averaged column density of  $\sim 10^{24}$  cm $^{-2}$ , above which the EW decreases again as the line-emitter becomes Compton-thick (e.g. see MY09). Increasing the covering factor of the reprocessor can increase the EW of the Fe K $\alpha$  line observed in reflection but there is a trade-off because as the covering factor approaches unity, the projected area of the reflection region decreases and emission-line photons are more prone to being impeded from escaping the medium. Ikeda et al. (2009) found that the EW is greatest for covering factors

factors of  $\sim 0.7 - 0.9$  but does not exceed  $\sim 180$  eV in their model for cosmic abundances and a power-law photon index of 1.9. In principle, the shape and relative magnitude of the Fe  $K\alpha$  line Compton shoulder could determine whether the reprocessor is Compton-thin or Compton-thick but this is challenging due to the limited signal-to-noise ratio of the data and also requires more sophisticated modeling. Such an investigation will be reported in future work. So far, all analyses with respect to the Compton shoulder and HEG AGN data have employed *ad-hoc* models (e.g. Kaspi et al. 2002; Yaqoob et al. 2005) so they do not yield a meaningful physical interpretation.

### 4.3. INTRINSIC LINE WIDTH

The location of the medium responsible for the core of the Fe  $K\alpha$  emission line can potentially be constrained by the measurements of the line intrinsic width. The weighted mean FWHM of the Fe  $K\alpha$  line cores for the 53 individual data sets (27 unique sources) for which it could be measured (Table 2), is  $2060 \pm 230$  km s<sup>-1</sup>. This includes the two sources (Mrk 290 and 4C 74.26) for which the Fe  $K\alpha$  line FWHM could only be constrained from the summed spectra. We also calculated the weighted mean FWHM from “per source” measurements and found a similar value of  $2200 \pm 220$  km s<sup>-1</sup> (see Table 3).

In Table 2 are values of the  $H_\beta$  FWHM compiled from the literature. Comparing the Fe  $K\alpha$  line FWHM with that of the  $H_\beta$  line can potentially give a direct indication of the location of the Fe  $K\alpha$  line-emitting region relative to the optical broad-line region. A direct comparison of the Fe  $K\alpha$  line width with optical BLR line widths was not attempted in YP04 because the number of sources with sufficiently high quality Fe  $K\alpha$  line-width measurements was too small. Nevertheless, Nandra (2006) using the YP04 results, supplemented by a few other HEG measurements from the literature, examined the relation between the FWHM of Fe  $K\alpha$  and  $H_\beta$ . The results were ambiguous, the data allowing for an origin of the Fe  $K\alpha$  line anywhere from the BLR to parsec-scale distances from the putative central black hole. Moreover, some of the HEG measurements for the Fe  $K\alpha$  line FWHM compiled from the literature were problematic. For example, for MR 2251–178, Gibson et al. (2005) reported an upper limit on the Fe  $K\alpha$  line FWHM of  $1530$  km s<sup>-1</sup> and Nandra et al. (2006) erroneously quoted and used as  $650$  km s<sup>-1</sup> (Gibson et al. 2005 reported a  $\sigma$  of  $650$  km s<sup>-1</sup>, not FWHM). In our uniform analysis, we found that the HEG data for MR 2251–178 were so poor that a meaningful upper limit on the Fe  $K\alpha$  FWHM cannot even be measured and therefore we have reported only results for a fit with the line width fixed at well below the HEG resolution (Table 1).

A notable example for which a meaningful comparison between the Fe  $K\alpha$  and  $H_\beta$  line widths has been reported using HEG data is NGC 7213 (Bianchi et al. 2008). In this case the FWHM of both lines are consistent with each other ( $\sim 2500 \text{ km s}^{-1}$ ), implying an origin of the Fe  $K\alpha$  line in the BLR for NGC 7213. Our sample includes NGC 7213 and our analysis (see Table 2) confirms the results of Bianchi et al. (2008). Utilizing all of the results from our uniform analysis of the HEG sample for which the Fe  $K\alpha$  line width could be at least loosely constrained (Table 2), we have plotted in Fig. 5 the Fe  $K\alpha$  line FWHM against the  $H_\beta$  FWHM. The dashed line corresponds to the two line widths being equal. The statistical errors shown correspond to 68% confidence. We have distinguished 12 sources in Fig. 5 by empty circles (as opposed to filled circles) that provide the very best statistical constraints on the Fe  $K\alpha$  line FWHM in our sample. The next best measurement of the FWHM would be NGC 985, but we note that its 99% two-parameter confidence contour for Fe  $K\alpha$  line flux versus FWHM did not close before the Gaussian component began to model the continuum. In Fig. 5, points that lie above the dashed line at some level of confidence mean that an origin in the BLR of at least part of the Fe  $K\alpha$  line is not ruled out, but contributions from further out than the BLR are not ruled out either (at the appropriate level of confidence). A larger FWHM for the Fe  $K\alpha$  line compared to the  $H_\beta$  line could either mean a genuine contribution to the Fe  $K\alpha$  line from matter closer to the central black hole than the BLR, or it could mean that there is a contribution from an unresolved Compton shoulder or from part of a broader disk line. Points that lie *below* the dashed line in Fig. 5 at some level of confidence place stronger constraints on the origin of the narrow Fe  $K\alpha$  line because in that case, whatever physical sources of broadening are affecting the Fe  $K\alpha$  line, it must originate in a region that lies further from the central black hole than BLR.

Standard tests for assessing the significance of any possible correlation between  $\text{FWHM}(\text{Fe } K\alpha)$  and  $\text{FWHM}(H_\beta)$ , such as the Spearman Rank correlation coefficient, are problematic because they do not take account of measurement errors on  $\text{FWHM}(\text{Fe } K\alpha)$ , which can be large. Assessing the effect of measurement errors on such correlation coefficients properly requires extensive and realistic simulations of the data *and* the spectral-fitting process. Instead, we used the  $\chi^2$  statistic to fit a straight line to the FWHM values of the Fe  $K\alpha$  and  $H_\beta$  lines. Although we are forced to assume a relationship between the two quantities, any correlation would still manifest itself. In the fitting we explicitly took into account the statistical errors on the Fe  $K\alpha$  line widths, using the average of the 68% confidence upper and lower errors. We found that  $\text{FWHM}(\text{Fe } K\alpha) = (0.04 \pm 0.13) \times \text{FWHM}(H_\beta) + (2130 \pm 550)$ , with  $\chi^2 = 17.1$  for 21 degrees of freedom. The reduced  $\chi^2$  value  $< 1$  then means that indeed a more complicated model is not warranted. More importantly, we see that even the  $1\sigma$  errors on the slope include a slope value of zero (corresponding to the case that all the FWHM values are consistent with a constant, independent of the FWHM of the  $H_\beta$  line). Therefore,

we find no evidence of a correlation between the Fe  $K\alpha$  and  $H\beta$  line widths, consistent with the conclusion of Nandra et al. (2006). However, Nandra et al. (2006) interpreted the lack of a correlations in terms of the narrow Fe  $K\alpha$  line not originating in the BLR, but we now know that in some cases this is not true (e.g. NGC 7213, Bianchi et al. 2008). We shall see below that our results in fact show that the location of the Fe  $K\alpha$  line emitter relative to the BLR appears to be genuinely different from source to source.

From our spectral fits to the subset of HEG data with the Fe  $K\alpha$  line width free (Table 2) we constructed joint 68%, 90%, 99% confidence contours of the Fe  $K\alpha$  line EW versus the *ratio* of the Fe  $K\alpha$  FWHM to the  $H\beta$  FWHM. These are shown in Fig. 6 and a variety of behavior is displayed. We found cases in which this FWHM ratio was, at the two-parameter 99% confidence level, was less than 1 (NGC 3783, NGC 4151 and NGC 5548), greater than 1 (MCG –6-30-15), or consistent with 1 (3C 120, NGC 2110, MCG –5-23-16, NGC 3516, NGC 5506, Mrk 509, NGC 7213, and NGC 7469). Thus, it appears that the location of the Fe  $K\alpha$  line relative to the location of the  $H\beta$  line-emitting region may be different from source to source. For our limited-sized sample the Fe  $K\alpha$  line-emitting region size could be up to a factor  $\sim 5$  larger than the  $H\beta$  line-emitting region (NGC 4151 – see Fig. 6). We note that the putative parsec-scale obscuring torus that is required by AGN unification schemes, and that has always been a strong contender for any Fe  $K\alpha$  line emission beyond the BLR, may be smaller than traditionally thought. In particular, Gaskell, Goosmann, & Klimek (2008) argue that there is considerable observational evidence that the BLR itself has a toroidal structure, and that there may be no distinct boundary between the BLR and the classical parsec-scale torus. Our results from the *Chandra* HEG data do not conflict with such a scenario.

From joint confidence contours of Fe  $K\alpha$  line intensity versus FWHM we can determine whether the line is resolved from a given data set if the contour (at some level of confidence) does not cross the FWHM = 0 axis. We found that at 99% confidence (two parameters), the *Chandra* HEG resolves the narrow component of the Fe  $K\alpha$  emission in 15 sources, namely, F9, NGC 2110, MCG –5-23-16, NGC 3516, NGC 3783, NGC 4051, NGC 4151, MCG –6-30-15, IRAS 13349+2438, IC 4329A, Mrk 279, NGC 5548, E1821+643, NGC 7469 and NGC 7213. We do not include PG 0834+346 here, since the single-Gaussian fit with the line width free does not pick up the narrow component at  $\sim 6.4$  keV (see §3). We caution that in general an emission line that is resolved by the HEG may indicate complexity as opposed to a simple, single emission line.

#### 4.4. LINE FLUX

If the Fe  $K\alpha$  line originates in a matter distribution whose light-crossing time is much greater than the typical timescale of variability of the X-ray continuum, the variability of the line flux will be suppressed. The line flux may then even be constant (within statistical errors) and correspond to some historically-averaged continuum level. The sources in our HEG sample that have multiple observations enable us to investigate the time-dependence of the Fe  $K\alpha$  line flux. The spectral resolution of the HEG currently allows the best isolation of the narrow Fe  $K\alpha$  line for the largest sample compared to previous studies. In Fig. 2 we showed the Fe  $K\alpha$  line intensity versus centroid energy 99%, two-parameter confidence contours for each source that has multiple observations. The contours for NGC 3783 were shown in Yaqoob et al. (2005) and are not shown again in Fig. 2. In no source did we find evidence for variability of the Fe  $K\alpha$  line flux at 99% confidence or greater. However, it is important to note that the 99% confidence regions in some cases cover a large range in line flux due to limited signal-to-noise ratio. However, we can say that in our HEG sample, the data are consistent with no variability of the Fe  $K\alpha$  line but more sensitive instrumentation is required to reduce the statistical errors.

### 5. X-RAY BALDWIN EFFECT

The so-called X-ray Baldwin effect, a possible anti-correlation between the Fe  $K\alpha$  line EW and X-ray luminosity, has been discussed at length in the literature (e.g. Iwasawa & Taniguchi 1993; Nandra et al. 1997; Page et al. 2004b; Jiang, Wang, & Wang 2006; Bianchi et al. 2007; Winter et al. 2009). These studies have found some evidence for an X-ray Baldwin effect albeit with significant scatter, but the latter two studies have found that the Fe  $K\alpha$  line EW appears to be more strongly anti-correlated with the ratio of X-ray luminosity to Eddington luminosity ( $L_x/L_{\text{Edd}}$ , a proxy for the accretion rate). However, Winter et al. (2009) found that the X-ray Baldwin effect was only significant if the EW and  $L_x/L_{\text{EDD}}$  values were binned, and the formal significance of the anti-correlation depended strongly on the details of the binning procedure. Except for some *HETGS* data used by Jiang et al. (2006), *all* other studies of the X-ray Baldwin effect to date have been based on data that has a spectral resolution of  $\sim 7000$  km s $^{-1}$  FWHM or worse. Therefore, it is not clear whether the Fe  $K\alpha$  line parameters in these studies correspond to contributions from line emission blended from completely different origins (e.g. distant-matter and accretion-disk components). Using our sample that consists *only* of HEG data, we can investigate the X-ray Baldwin effect with a spectral resolution in the Fe K band that is nearly four times better than in previous studies, and therefore provide the best isolation of the narrow core that is



possible with current instrumentation.

For this purpose we used our spectral-fitting results obtained with the Fe K $\alpha$  line width fixed at 1 eV, well below the HEG resolution, in order to obtain a uniform set of Fe K $\alpha$  line EW measurements for the largest number of sources (see Table 1). We examined correlations using both the “per observation” results and the “per source” results. Measurements for the latter were derived from only one spectrum per source, which in some cases was the average spectrum, as described in §4. These values of EW are plotted against  $L_x$  in Fig. 7(a) and Fig. 7(c), and against  $L_x/L_{\text{EDD}}$  in Fig. 7(b) and Fig. 7(d). Note that in Fig. 7 we have shown all EW measurements whether or not they are only upper limits, even though upper limits will not be used in the quantitative analysis. The Eddington luminosity,  $L_{\text{Edd}}$ , is computed from  $M_{\text{BH}} \times 1.3 \times 10^{38} \text{ erg s}^{-1}$ , where  $M_{\text{BH}}$  is the mass of the central black hole. Values of  $M_{\text{BH}}$  are from Zhou & Wang (2005), Bianchi et al. (2007), and Wang et al. (2009). As a proxy for the accretion rate we use the ratio of  $L_{2-10\text{keV}}/L_{\text{Edd}}$  (see e.g. Vasudevan & Fabian 2009 for the correspondence between X-ray luminosity and bolometric luminosity). We were not able to find reliable mass estimates for Mrk 705 and IRAS 18325–5926 so these sources were excluded from any analyses involving  $L_{\text{Edd}}$ . The statistical errors shown in Fig. 7 are 68% confidence for two free (Gaussian) parameters. It can be seen that, despite better isolation of the Fe K $\alpha$  line core, there is still significant scatter in the diagrams.

In order to formally assess the significance of any correlation, standard methods that do not take account of the statistical errors on the EW, such as the Spearman Rank correlation coefficient are problematic. This is because, in the type of analysis presented here, and in previous works on the X-ray Baldwin effect, the actual best-fitting values of EW are not in themselves meaningful. It is the statistical errors on the EW that are the important quantities. Assessing the effect of measurement errors on such correlation coefficients properly requires extensive and realistic simulations of the data *and* the spectral-fitting process. On the other hand, the  $\chi^2$  statistic does take account of the statistical errors on the EW. Although we are forced to assume a form of the relationship between the EW and  $L_x$  if we use  $\chi^2$ , it can be seen from Fig. 7 that the quality of the data do not support constraining a more complex relationship. We therefore fitted a straight line to  $\log EW$  versus  $\log L_x$  using the  $\chi^2$  fit statistic (i.e. a power-law function for EW versus  $L_x$ ). Data points that only had upper limits on the EW were *not* included. In the fitting we took into account the statistical errors on the EW, using the average of the 68% confidence upper and lower errors.

The results of the  $\chi^2$  analysis are shown in Table 4. For each of the four cases (“per observation”, “per source”, and EW versus  $L_x$  or  $L_x/L_{\text{Edd}}$ ) we show the best-fitting value of  $\chi^2$ , the intercept and slope of the best-fitting line, as well as the the 68% confidence and

99% confidence one-parameter errors on the slope. The latter error bounds were determined by varying the slope, whilst allowing the intercept to float, and determining the bounds on the slope for  $\Delta\chi^2 = 0.989$  and  $6.635$  for 68% and 99% confidence respectively. If the EW is indeed anti-correlated with either  $L_x$  or  $L_x/L_{\text{Edd}}$  we would expect that the slope of the line is significantly different from zero. Therefore, in Table 4 we also show values of  $\Delta\chi^2$  obtained when the slope is forced to be zero, as well as the corresponding significance that the slope is non-zero. We found that the “per observation” results gave a stronger anti-correlation than the “per source” results, for both the EW versus  $L_x$  and EW versus  $L_x/L_{\text{Edd}}$  relations. Quantitatively, the “per observation” results show a significance of  $6.05 - 6.27\sigma$  for a non-zero slope, as opposed to  $\sim 3.08 - 3.24\sigma$  for the “per source” results. The best-fitting slopes for the latter are about half of the corresponding values of the “per observation” results. We caution that the absolute significance values should not be interpreted literally since we do not know the form of the functional relationship between EW and  $L_x$ . Table 4 also shows that there is no significant difference in the  $\chi^2$  analysis results on whether we examine the relation of EW between  $L_x$  or  $L_x/L_{\text{Edd}}$ , and that is true whether we consider the “per observation” or “per source” results. Both our “per observation” and “per source” results for the slope of the EW versus  $L_x$  relation are formally consistent, within the uncertainties, with that found by Page et al. (2004b) who reported  $EW \propto L^{-0.17 \pm 0.08}$ . In addition, our results for the slope of the relation between EW and  $L_x/L_{\text{Edd}}$  is formally consistent with that obtained by Bianchi et al. (2007) ( $EW \propto (L_{\text{bol}}/L_{\text{Edd}})^{-0.19 \pm 0.05}$ ). We note that the latter study of Bianchi et al. (2007) excluded sources with high radio-loudness and still found a significant Baldwin effect.

Our results seem to confirm the X-ray Baldwin effect. There are several factors that could produce an anti-correlation of the EW of the Fe  $K\alpha$  line and the intrinsic X-ray continuum luminosity. A decrease of covering factor and/or the column density of line-emitting with increasing X-ray continuum luminosity likely are the most important factors. Another possibility is that the line-emitting material becomes more and more ionized as the X-ray luminosity increases, leaving less low-ionization material to produce the Fe  $K\alpha$  line at  $\sim 6.4$  keV. Unfortunately the data cannot yet distinguish between these scenarios. A complete understand of the Baldwin effect should also take into consideration the fact that the Fe  $K\alpha$  line EW in individual sources can vary by more than a factor of two (if the line intensity does not respond to large-amplitude continuum variations), although simulations based on the simplest assumptions yield an anti-correlation between EW and continuum luminosity weaker than observed ones and with large scattering ( $EW \propto L^{-0.05 \pm 0.05}$ , Jiang et al. 2006).

## 6. SUMMARY

We have presented an empirical and uniform analysis of the narrow core of the Fe  $K\alpha$  emission line in a sample of 82 observations of 36 AGNs with low to moderately low X-ray absorption ( $N_H < 10^{23} \text{ cm}^{-2}$ ), using *Chandra* HEG data. The Fe  $K\alpha$  line was detected in 33 sources, and its centroid energy was measured in 32 sources (68 observations). The distribution in the centroid energy is strongly peaked around  $\sim 6.4$  keV, with over 80% of the measurements lying in the range 6.38–6.43 keV. Including the statistical errors and utilizing the best measurements for each source, the line centroid energy lies entirely in the range 6.35–6.47 keV for 30 out of 32 sources. Thus we confirm, for the largest sample of AGN observed with such a high spectral resolution (FWHM  $\sim 1860 \text{ km s}^{-1}$  at 6.4 keV), the ubiquity of the narrow core of Fe  $K\alpha$  line, and its preferred origin in cool, neutral or only mildly-ionized matter.

The equivalent width (EW) of the core of the Fe  $K\alpha$  line was constrained in 70 out of 82 observations, with only upper limits obtained from the remaining 12 spectra. The weighted mean EW was  $53 \pm 3$  eV, and  $\sim 70\%$  of the individual measurements had a 68% confidence upper limit on the EW of less than 100 eV. Similar results were obtained when considering the EW distribution by source, although the weighted mean was somewhat higher from measurements that allowed the intrinsic line width to be free ( $70 \pm 4$  eV). The EW distribution can be produced by both Compton-thin and Compton-thick matter distributions and a more detailed analysis with a physical model is required to distinguish between the two scenarios. We also presented measurements of the flux of the core of the Fe  $K\alpha$  line and found that for sources that had multiple observations, there was no case in which the line flux varied between observations, within the statistical errors.

The intrinsic width of the core of the Fe  $K\alpha$  line was measured for 27 sources (53 observations) and we obtained a weighted mean value of FWHM =  $2060 \pm 230 \text{ km s}^{-1}$  (or =  $2200 \pm 220 \text{ km s}^{-1}$  when considering measurements by source, not by observation). Of the 27 sources, 12 yielded 99% confidence, two-parameter contours of line flux versus FWHM that were good enough to investigate the relation between the width of the Fe  $K\alpha$  line and the width of the H $\beta$  line (or Br $\alpha$  for one of the sources). We found that the ratio of the X-ray to optical line width varies from source to source. The 99% confidence, two-parameter upper limit lies in the range  $\sim 0.5 - 4$  for the 12 sources. This means that contributions to the flux of the core of the Fe  $K\alpha$  line are allowed down to a factor  $\sim 0.7 - 2$  times the radius of the optical BLR. The upper limit on the size of the X-ray line emitter is not constrained because line flux contributions from large, parsec-scale distances could be unresolved by the HEG. We note that our results are suggestive of the fact that the location of the X-ray line-emitting region relative to the BLR may actually be different in different sources. These

conclusions are subject to the caveat that derivation of the true velocity width of the Fe  $K\alpha$  line core requires a proper physical model, such as that of MY09, that includes a possible Compton shoulder. This will be the subject of future work. However, we note that such an analysis can only reduce the derived velocity widths of the Fe  $K\alpha$  lines. Finally, having isolated the narrow core of the Fe  $K\alpha$  line with the best available spectral resolution we confirm the anti-correlation (albeit with a large scatter) between the line EW and X-ray luminosity,  $L_x$  (the X-ray Baldwin effect), and between the line EW and  $L_x/L_{\text{Edd}}$ .

We thank the referee for his/her useful comments. Partial support for this work was provided by NASA through *Chandra* Award AR8-9012X, issued by the Chandra X-ray Observatory Center, which is operated by the Smithsonian Astrophysical Observatory for and on behalf of the NASA under contract NAS8-39073. X.W.S. and J.X.W. acknowledge support from Chinese National Science Foundation (Grant No. 10825312, 10773010), and Knowledge Innovation Program of CAS (Grant No. KJCX2-YW-T05). This research made use of the HEASARC online data archive services, supported by NASA/GSFC. This research has made use of the NASA/IPAC Extragalactic Database (NED) which is operated by the Jet Propulsion Laboratory, California Institute of Technology, under contract with NASA. The authors are grateful to the *Chandra* instrument and operations teams for making these observations possible.

## 7. APPENDIX: NOTES ON INDIVIDUAL SOURCES

In this section we give, for each source in our sample, particular additional details of the analysis and/or results where necessary. We also summarize briefly any previously-published HEG results in the Fe K band that are based on the same data. Our intention is not to review observations by other instruments.

*F9.* Chandra HEG results were reported in YP04 and the new analysis is consistent with the previous results. Note that the very large upper limit on the intrinsic Fe  $K\alpha$  line width (Table 2) is unphysical since such a broad Gaussian component is clearly modeling the underlying spectrum (see discussion in YP04). The HEG data show marginal evidence of an emission line at  $\sim 6.9$  keV.

*NGC 526a.* No results from either of the two observations have been previously published. The Fe  $K\alpha$  line is detected in only one of the observations, and the detection is marginal. Consequently, the FWHM of the line could not be constrained.

*Mrk 590.* Results from the *Chandra* HEG data have been presented by Longinotti et al. (2007), who reported the detection of a narrow Fe  $K\alpha$  line with  $E_0 = 6.40_{-0.03}^{+0.04}$  keV,

$\sigma_{\text{Fe K}} = 47_{-24}^{+58}$  eV, and  $\text{EW} = 160_{-78}^{+118}$  eV. Our best-fitting Fe K $\alpha$  line parameters (Table 1) are in good agreement with those measured by Longinotti et al. (2007). Fig. 1 shows that the large 99% confidence region for  $I_{\text{Fe K}}$  versus  $E_0$  indicates that the fits in which the line width was free do not provide a reliable measure of the intrinsic line width.

*NGC 985.* Although Krongold et al. (2005) reported results from the *Chandra HETGS* observation, they combined HEG and MEG data and did not report results on the Fe K $\alpha$  line emission.

*ESO 198–G24.* No results from any of the two *Chandra HETGS* observations have been previously reported. We obtained a significant detection of the narrow Fe K $\alpha$  line from only one of the observations (Table 1 and Table 2).

*3C 120.* Results on the Fe K $\alpha$  line from the *Chandra HETGS* observation of this source have been reported in YP04 and the new results presented here are consistent with the previous ones. The HEG data show a marginal detection of an emission line at  $\sim 6.9$  keV (YP04).

*NGC 2110.* The results from the four *Chandra HETGS* observations were presented by Evans et al. (2007), who measured the narrow Fe K $\alpha$  line parameters  $E_0 = 6.397 \pm 0.007$  keV, and  $\text{EW} = 81_{-30}^{+27}$  eV, consistent with our results. Note that in the second observation the line width could not be constrained so the  $I_{\text{Fe K}}$  versus  $E_0$  99% confidence contour for that observation in Fig. 2 was constructed with the line width fixed at 1 eV (dot-dashed line).

*PG 0844+349.* No results from any of the three *Chandra HETGS* observations of this source have been reported previously. The detection of the Fe K $\alpha$  line at  $\sim 6.4$  keV is marginal, and there is also marginal evidence of emission lines due to He-like and H-like Fe. When fitted with a single-Gaussian model, the presence of three narrow emission lines causes the Gaussian intrinsic width to become large as it tries to account for all three lines. Therefore, the most reliable values of  $E_0$  and  $I_{\text{Fe K}}$  are those obtained from fits in which the line width was fixed.

*MCG –5-23-16.* This source was observed by the *Chandra HETGS* on three occasions. Results from the first observation have been presented by Balestra et al. (2004), who found, from single-Gaussian fits to the narrow Fe K $\alpha$  line,  $E_0 = 6.38 \pm 0.02$  keV,  $\text{EW} = 70 \pm 28$  eV, and  $\text{FWHM} \leq 6500 \text{ km s}^{-1}$  (at 99% confidence). Results from the remaining two observations were presented by Braitto et al. (2007), who reported Fe K $\alpha$  narrow-line parameters for the mean (time-averaged) spectrum of  $E_0 = 6.41_{-0.01}^{+0.02}$  keV, and  $\text{EW} = 61_{-23}^{+17}$  eV. These correspond to the case when the line width was fixed at a value less than the instrument resolution and Braitto et al. (2007) found that if the line width was allowed to float, the constraints were sensitive to details of the continuum and relativistic disk-line model. Our results are

consistent with previously published results; our simple continuum model and omission of a broad relativistic line in the fits means that our measurements of the line width should be interpreted as empirical indicators only. Note that in the second observation the 99% confidence contour of the Fe K $\alpha$  line intensity versus energy was not closed when the line width was a free parameter. Thus, for this observation, we show in Fig. 2 the 99% confidence contour for the line width fixed at 1 eV (thin solid line).

*Mrk 705.* The signal-to-noise ratio of the data in this observation was very poor. Previous results have been reported by Gallo et al. (2005) who obtained an upper limit of 149 eV on the EW of an emission line with a centroid energy fixed at 6.4 keV. This is consistent with our analysis (Table 1).

*NGC 3227.* Results from the *Chandra HETGS* observation of this source have been reported in YP04 and the new results presented here are consistent with the previous ones.

*NGC 3516.* There were eight *Chandra HETGS* observations of this source. Results from the first three observations were reported in YP04. In the present paper we report on the analysis of five new observations that were performed in October 2006. Results from the same datasets have also been presented by Turner et al. (2008), who reported the detection of a narrow Fe K $\alpha$  emission line with  $E_0 = 6.404 \pm 0.019$  keV,  $\sigma_{\text{Fe K}} = 40_{-15}^{+10}$  eV, and EW  $\sim 94$  eV (the statistical error was not given). In addition, redshifted emission-line features have been reported in some of the HEG data (Turner et al. 2002), as well as H-like and He-like Fe emission and absorption features (Turner et al. 2008). In the present paper we are concerned only with the Fe K $\alpha$  emission line centered at  $\sim 6.4$  keV and our results are consistent with those of Turner et al. (2008). Due to the short exposure time of the last observation, the Fe K $\alpha$  line was detected at less than 99% confidence (for two free Gaussian parameters). Thus, we do not show the contour of the line intensity versus energy in Fig. 2 for this observation.

*NGC 3783.* Detailed results from the six *Chandra HETGS* observations of this source have been presented by Yaqoob et al. (2005), and Kaspi et al. (2001, 2002) and our re-analysis is consistent with the previous results.

*NGC 4051.* Results from the *Chandra HETGS* observation of this source have been reported by Collinge et al. (2001), who obtained  $E_0 = 6.41_{-0.01}^{+0.01}$  keV, EW =  $158_{-47}^{+51}$  eV, and FWHM  $< 2800$  km s $^{-1}$  for the core of the narrow Fe K $\alpha$  line. Our analysis is consistent with the previous results, except that when the line width was free in the fits it becomes larger than the narrow core in the data (Table 2), and this is consistent with the results reported in YP04. Absorption features due to He-like and H-like Fe have also been noted in the HEG data for NGC 4051 (Collinge et al. 2001; YP04).

*NGC 4151.* This source was observed five times with the *Chandra HETGS*. Results from the first observation have been reported by Ogle et al. (2000) who obtained  $EW = 160 \pm 20$  eV, consistent with our measurement (Table 1) and a FWHM of  $1800 \pm 200$  km s<sup>-1</sup>, also consistent with our analysis (Table 2). The line centroid energy was not measured. Results for narrow Fe K $\alpha$  line parameters measured by the HEG for the remaining four observations have not been previously published.

*Mrk 766.* Results for the *Chandra HETGS* observation of this source have been reported in YP04 and our re-analysis is consistent with the previous results. The HEG data show marginal evidence of an emission line at  $\sim 6.9$  keV (YP04).

*3C 273.* A narrow Fe K $\alpha$  line was detected in only one of the 7 *Chandra HETGS* observations of this source. Measurements of the Fe K $\alpha$  line core from *Chandra* HEG data have not been previously reported.

*NGC 4593.* Results for the *Chandra HETGS* observation of this source have been reported in YP04 and our re-analysis is consistent with the previous results. The HEG data show marginal evidence of an emission line at  $\sim 6.9$  keV (YP04).

*MCG –6-30-15.* This source was observed by the *Chandra HETGS* five times. Results from the first observation have been presented by Lee et al. (2002) and YP04. The results for the other four observations were presented by Young et al. (2005), who reported narrow Fe K $\alpha$  emission-line parameters from the time-averaged spectrum of  $E_0 = 6.393_{-0.014}^{+0.106}$  keV,  $EW = 18_{-8}^{+11}$  eV, and a FWHM  $< 4700$  km s<sup>-1</sup>. In the present analysis, only one out of four new observations had a significant detection of the narrow Fe K $\alpha$  emission line. From our empirical analysis we obtained a larger EW and FWHM than Young et al. (2005). This could be attributed to a contribution to the Fe K $\alpha$  line core from an underlying disk-line component and/or the difference could be due to a complex continuum. However, there is a large range of possible models but in our analysis the simple empirical model is appropriate because the results can be compared directly to those from the other sources in our sample. The EW and FWHM obtained from more complex models will always be less than the values obtained from the empirical modeling so the latter provide useful upper bounds. He-like and H-like Fe absorption features have been reported in the HEG data by Young et al. (2005).

*IRAS 13349+2438.* This source was observed twice with the *Chandra HETGS* but no results for the Fe K $\alpha$  line have been previously published. A significant detection of the narrow Fe K $\alpha$  line was obtained only from the second observation (see Table 1).

*IC 4329A* McKernan & Yaqoob (2004) reported the detection of complex Fe K line emission from the *Chandra HETGS* observation of this source. One peak is centered at  $\sim 6.3$  keV with a FWHM  $20830_{-7375}^{+10110}$  km s<sup>-1</sup> and an EW of  $110_{-40}^{+46}$  eV. The other peak

is at  $\sim 6.9$  keV with a FWHM  $\sim 4000$  km s $^{-1}$  and an EW of  $\sim 40$  eV (probably due to Fe XXVI Ly $\alpha$ ). In the present analysis we are concerned only with the low-ionization Fe K $\alpha$  line. Our re-analysis with the line width free is consistent with the results of McKernan & Yaqoob (2004) but we note that our fits in which the Fe K $\alpha$  line width was fixed at well below the HEG resolution yielded a line centroid energy of  $6.399^{+0.006}_{-0.005}$  keV. Therefore the Fe K $\alpha$  line parameters from the latter fit are more reliable values for the true narrow core of the Fe K $\alpha$  line.

*Mrk 279.* Results of the new analysis for this source are consistent with those reported in YP04.

*NGC 5506.* Results from the *Chandra HETGS* observation of this source have been presented by Bianchi et al. (2003), who obtained FWHM  $< 4000$  km s $^{-1}$  for the narrow Fe K $\alpha$  line at  $\sim 6.4$  keV at 99% confidence. We obtained a tighter limit on the FWHM (Table 2). Bianchi et al. (2003) did not provide constraints on the line centroid energy or EW.

*NGC 5548.* Results for both of the *Chandra HETGS* observations have already been reported in Yaqoob et al. (2001) and YP04, and the new analysis is consistent with the previous results.

*Mrk 290.* There are four *Chandra HETGS* observations for this source and no results on the Fe K $\alpha$  line from the HEG data have previously been published. None of the individual observations yielded a detection of the narrow Fe K $\alpha$  line greater than 99% confidence (for two free parameters). However, the line was detected with  $> 3\sigma$  confidence in the time-averaged spectra. The line intensity against centroid energy confidence contours shown in Fig. 2 were obtained with the line width fixed at 1 eV since a closed 99% confidence contour could not be obtained when the line width was a free parameter.

*PDS 456.* Results from the *Chandra HETGS* observation of this source pertaining to the narrow Fe K $\alpha$  line have never been previously published. The signal-to-noise ratio is poor and we could only obtain upper limits on the EW after fixing the line energy at 6.4 keV.

*E1821+643.* Results from the *Chandra HETGS* observation of this source have been presented by Fang et al. (2002) and Yaqoob & Serlemitsos (2005). The latter work reported Fe K $\alpha$  line parameters  $E_0 = 6.43^{+0.06}_{-0.05}$  keV,  $EW = 144^{+67}_{-57}$  eV, and  $FWHM = 10980^{+3300}_{-7690}$  km s $^{-1}$ . However, as described in Yaqoob & Serlemitsos (2005), these parameters are quite model-dependent because an absorption line was reported at  $\sim 6.2$  keV in the rest frame, and there may also be an underlying broad emission line. Our fits with the line width fixed at 1 eV likely give the most representative values of the centroid energy and EW of the narrow core of the Fe K $\alpha$  line.



*3C 382.* Gliozzi et al. (2007) have presented the results from the two *Chandra HETGS* observations of this source. The Fe K $\alpha$  line was detected with less than 90% and less than 99% confidence in first and second observations, respectively. From the second observation Gliozzi et al. (2007) obtained  $E_0 = 6.43_{-0.07}^{+0.05}$  keV,  $EW = 55_{-20}^{+47}$  eV, and  $FWHM < 9560$  km s $^{-1}$ . Our results are generally consistent with those of Gliozzi et al. (2007), but we note that the latter work also reported results from the  $-1$  and  $+1$  orders of the HEG separately, giving a larger dispersion in the parameter ranges.

*IRAS 18325–5926* and *4C 74.26.* No results from the *Chandra HETGS* observations (pertaining to the Fe K $\alpha$  line or otherwise) for either of these sources have been previously published. In IRAS 18325–5926 our analysis revealed no significant detection of the narrow Fe K $\alpha$  line in either of the two observations or from the summed spectrum. The detection of the line in 4C 74.26 was marginal even for the spectrum summed over two observations. Only upper limits on the EW could be derived for IRAS 18325–5926 (with the Fe K $\alpha$  line energy fixed at 6.4 keV).

*Mrk 509.* Results from the *Chandra HETGS* observation of this source have been reported in YP04 and the new analysis gives consistent results.

*NGC 7213.* Results from the two *Chandra HETGS* observations of this source have been reported by Bianchi et al. (2008). The narrow Fe K $\alpha$  line parameters obtained were  $E_0 = 6.397_{-0.011}^{+0.006}$  keV,  $EW = 120_{-30}^{+40}$  eV, and  $FWHM = 2400_{-600}^{+1100}$  km s $^{-1}$ . Our results are consistent with those of Bianchi et al. (2008), who also reported the detection of Fe XXV and Fe XXVI Ly $\alpha$  emission lines in the HEG data.

*NGC 7314.* Complex Fe K line emission from multiple ionization states was observed by the *Chandra HETGS*, and the results of a detailed analysis were published by Yaqoob et al. (2003). The Fe K $\alpha$  line at  $\sim 6.4$  keV is unresolved with  $FWHM < 3520$  km s $^{-1}$  and  $EW = 81 \pm 34$  eV. The results presented in the present paper (Table 1) were obtained from fits with the line width fixed at 1 eV. Emission lines from Fe XXV and Fe XXVI Ly $\alpha$  have been noted and discussed in detail by Yaqoob et al. (2003).

*Ark 564.* Results pertaining to the narrow Fe K $\alpha$  line from the *Chandra HETGS* observation have been presented by Matsumoto, Leighly, & Marshall (2004) and YP04. The signal-to-noise ratio of the data is poor and the EW of the line could only be measured with the line energy fixed at 6.4 keV and the line width fixed at 1 eV, and the results are consistent with those of YP04 (Table 1).

*MR 2251–178.* Gibson et al (2005) reported results from a *Chandra* observation, giving  $EW = 25 \pm 13$  eV and  $FWHM < 1530$  km s $^{-1}$  for an Fe K $\alpha$  line with a centroid energy fixed at 6.4 keV. In our uniform analysis, we found that the line was detected at less than 99%

confidence. In this case we were not able to obtain constraints on the line width. Gibson et al. (2005) also reported the detection of a resolved Fe XXVI Ly $\alpha$  absorption line with EW  $\sim$  28 eV and a velocity shift of  $\sim -12700$  km s $^{-1}$ , indicating a high-velocity outflow.

*NGC 7469*. Results from the two *Chandra HETGS* observations have been reported by Scott et al. (2005). A strong Fe K $\alpha$  line was detected with a centroid energy of  $6.39 \pm 0.01$  keV, and a line width  $6310 \pm 1580$  km s $^{-1}$ . No EW was given but the line flux was  $3.9 \pm 0.7 \times 10^{-5}$  photons cm $^{-2}$  s $^{-1}$ . Our results are consistent (within the statistical errors) with those of Scott et al. (2005).

## REFERENCES

- Arnaud, K. A., 1996, *Astronomical Data Analysis Software and Systems V*, eds. Jacoby, G., & Barnes, J., p. 17, ASP Conference Series, Vol. 101
- Balestra I., Bianchi S., Matt G., 2004, *A&A*, 415, 437
- Ballantyne, D., Fabian, A. C., 2005, *ApJ*, 622, L97
- Bianchi S., Balestra I., Matt G., Guainazzi M., Perola G. C., 2003, *A&A*, 402, 141
- Bianchi S., La Franca F., Matt G., Guainazzi M., Jiménez-Bailón E., Longinotti A. L., Nicastro F., Pentericci L., 2008, *MNRAS*, 389, 52
- Bianchi S., Guainazzi M., Matt G., Fonseca Bonilla, N., 2007, *A&A*, 467, L19
- Bianchi S., Guainazzi M., Matt G., Fonseca Bonilla N., Ponti G., 2009, *A&A*, 495, 421
- Bianchi S., Matt G., Nicastro F., Porquet D., Dubau J., 2005, *MNRAS*, 357, 599
- Braito V., Reeves J. N., Dewangan G. C. et al. 2007, *ApJ*, 670, 978
- Collinge M. J., Brandt W. N., Kaspi, S. et al. 2001, *ApJ*, 557, 2
- Evans D. A., Lee J. C., Turner T. J., Weaver K. A., Marshall H. L., 2007, *ApJ*, 671, 1345
- Fang T., Davis D. S., Lee J. C., Marshall H. L., Bryan G. L., Canizares C. R., 2002, *ApJ*, 565, 86
- Fang T., Marshall H. L., Bryan G. L., Canizares C. R., 2001, *ApJ*, 555, 356
- Gallo L. C., Balestra I., Costantini E., Boller Th., Burwitz V., Ferrero E., Mathur S., 2005, *A&A*, 442, 909

- Gaskell C. M., Goosmann R. W., Klimek E. S., 2008, *MmSAI*, 79, 1090
- Ghisellini G., Haardt F., Matt G., 1994, *MNRAS*, 267, 743
- Gibson R. R., Marshall H. L., Canizares, C. R., Lee J. C., 2005, *ApJ*, 627, 83
- Giozzi M., Sambruna R. M., Eracleous M., Yaqoob, T., 2007, *ApJ*, 664, 88
- Grandi P., Palumbo G. G. C., 2007, *ApJ*, 659, 235
- Guainazzi M., Bianchi S., Dovčiak M., 2006, *AN*, 327, 1032
- Ikeda S., Awaki H., Terashima, Y., 2009, *ApJ*, 692, 608
- Iwasawa K., Taniguchi Y., 1993, *ApJ*, 413, L15
- Jiang P., Wang J. X., Wang T. G., 2006, *ApJ*, 644, 725
- Kaspi S., Brandt W. N., Netzer, H. et al. 2001, *ApJ*, 554, 216
- Kaspi S., Brandt W. N., George, I. M. et al. 2002, *ApJ*, 574, 643
- Krongold Y., Nicastro F., Elvis M., Brickhouse N. S., Mathur S., Zezas A., 2005, *ApJ*, 620, 165
- Lee J. C., Iwasawa K., Houck J. C., Fabian A. C., Marshall H. L., Canizares C. R., 2002, *ApJ*, 570, L47
- Levenson N. A., Heckman T. M., Krolik J. H., Weaver K. A., Życki P. T., 2006, *ApJ*, 648, 111
- Longinotti A. L., Bianchi S., Santos-Lleo M., Rodríguez-Pascual P., Guainazzi M., Cardaci M., Pollock A. M. T., 2007, *A&A*, 470, 73
- Lubiński P., Zdziarski A. A., 2001, *MNRAS*, 323, L37
- Markert T. H., Canizares C. R., Dewey D., McGuirk M., Pak C., Shattenburg M. L., 1995, *Proc. SPIE*, 2280, 168
- Matsumoto C., Leighly K. M., Marshall H. L., 2004, *ApJ*, 603, 456
- Mendoza C., Kallman T. R., Bautista M. A., Palmeri P., 2004, *A&A*, 414, 377
- Miller J. M., 2007, *ARA&A*, 45, 441
- McKernan B., Yaqoob T., 2004, *ApJ*, 608, 157

- Murphy K., Yaqoob T., 2009, MNRAS, 397, 1549 (MY09)
- Nandra K., 2006, MNRAS, 368, L62
- Nandra K., George I. M., Mushotzky R. F., Turner T. J., Yaqoob T., 1997, ApJ, 488, L91
- Nandra K., O’Neill P. M., George I. M., Reeves J. N., 2007, MNRAS, 382, 194
- Ogle P. M., Marshall H. L., Lee J. C., Canizares C. R., 2000, ApJ, 545, L81
- Page K. L., O’Brien P. T., Reeves J. N., Turner M. J. L., 2004b, MNRAS, 347, 316
- Page K. L., Turner M. J. L., Done C., O’Brien P. T., Reeves J. N., Sembay S., Stuhlinger, M., 2004a, MNRAS, 349, 57
- Palmeri P., Mendoza C., Kallman T. R., Bautista M. A., Melendez M., 2003, A&A, 410, 359
- Perola G. C., Matt G., Cappi M., Fiore F., Guainazzi M., Maraschi L., Petrucci P. O., Piro, L., 2002, A&A, 389, 802
- Pike C. D., Phillips K. J. H., Lang J. et al. 1996, ApJ, 464, 487
- Scott J. E., Kriss G. A., Lee J. C. et al. 2005, ApJ, 634, 193
- Sulentic J. W., Marziani P., Zwitter T., Calvani M., Dultzin-Hacyan, D., 1998, ApJ, 501, 54
- Turner, T. J., Mushotzky R. F., Yaqoob T. et al. 2002, ApJ, 574, L123
- Turner T. J., Reeves J. N., Kraemer S. B., Miller L., 2008, A&A, 483, 161
- Turner T. J., Miller L., 2009, A&ARv, 17, 47
- Vasudevan R. V., Fabian A. C., 2009, MNRAS, 392, 1124
- Verner D. A., Ferland G. J., Korista K. T., Yakovlev D. G., 1996, ApJ, 465, 487
- Wang, J., Mao, Y. F., & Wei, J. Y., 2009, AJ, 137, 3388
- Weaver K. A., Gelbord J., Yaqoob T., 2001, ApJ, 550, 261
- Winter L. M., Mushotzky R. F., Reynolds C. S., Tueller J., 2009, ApJ, 690, 1322
- Yaqoob T., George I. M., Nandra K., Turner T. J., Serlemitsos P. J., Mushotzky R. F., 2001, ApJ, 546, 759

- Yaqoob T., George I. M., Kallman T. R., Padmanabhan U., Weaver. K. A., Turner T. J., 2003, ApJ, 596, 85
- Yaqoob T., Padmanabhan U., 2004, ApJ, 604, 63 (YP04)
- Yaqoob T., Reeves J. N., Markowitz A., Serlemitsos P. J., Padmanabhan U., 2005, ApJ, 627, 156.
- Yaqoob T., Serlemitsos P. J., 2005, ApJ, 623, 112
- Young A. J., Lee J. C., Fabian A. C., Reynolds C. S., Gibson R. R., Canizares C. R., 2005, ApJ, 631, 733
- Young A. J., Nowak M. A., Markoff S., Marshall H. L., Canizares C. R., 2007, ApJ, 669, 830
- Zhou X.-L., Wang J.-M., 2005, ApJ, 618, L83

## Figure Captions

### Figure 1

*Left Panels:* *Chandra* HEG spectra in the Fe K band for sources in which the Fe  $K\alpha$  emission line was detected in only one observation, and which were not included in the sample of Yaqoob & Padmanabhan (2004). The data are binned at  $0.01\text{\AA}$ , comparable to the HEG spectral resolution, which is  $0.012\text{\AA}$  FWHM. The data are combined from the  $-1$  and  $+1$  orders of the grating. The spectra have been corrected for instrumental effective area and cosmological redshift. Note that these are *not* unfolded spectra and are therefore independent of any model that is fitted. Although the spectral fitting was performed using XSPEC, the spectral plots were *not* made using XSPEC. The statistical errors shown correspond to the  $1\sigma$  Poisson errors, which we calculated using equations (7) and (14) in Geherls (1986) that approximate the upper and lower errors respectively. The solid line corresponds to a continuum model fitted over the 2–7 keV range (extrapolated to 7.5 keV), as described in the text (§3). The vertical dotted lines represent (from left to right), the rest energies of the following: Fe I  $K\alpha$ , Fe XXV forbidden, two intercombination lines of Fe XXV, Fe XXV resonance, Fe XXVI Ly $\alpha$ , Fe I  $K\beta$ , and the Fe K edge. *Right Panels:* Joint 99% confidence contours of the Fe  $K\alpha$  emission-line core intensity versus line centroid energy obtained from Gaussian fits to the line with the line width free as described in the text (solid lines). For Mrk 590, NGC 985, PG 0844+346(1) and IRAS 13349+2438(2), the 99% confidence contours (solid lines) of the were poorly constrained due to the intrinsic line width parameter becoming very large. Therefore, we overlaid the 99% confidence contours obtained with the line width fixed at 1 eV for these cases (dotted contours). For the remaining sources (ESO 198–G24, MCG –6-30-15(2), NGC 5506, and E1821+643), the dotted contours correspond to 68%, and 90% confidence.

### Figure 2

*Left Panels:* The time-averaged *Chandra* HEG spectra in the Fe K band for eight AGN in which the Fe  $K\alpha$  emission line was detected in more than one observation for cases that were not already reported in Yaqoob & Padmanabhan (2004). The data are binned at  $0.01\text{\AA}$  except for NGC 4151, which is binned at  $0.005\text{\AA}$ . The energies of the vertical dotted lines are described in the caption to Fig. 1. *Right Panel* Joint 99% confidence contours of the Fe  $K\alpha$  emission-line core intensity versus line center energy for time-averaged and individual spectra. Individual observations are shown in different linestyles while the time-averaged contours are shown with a solid line. The contour shown for Mrk 290 is from the time-averaged spectrum only, since none of the individual observations had sufficient signal-to-noise ratio to obtain well-constrained contours. For MCG –6-30-15, we show the contour from the time-averaged spectrum only, since only one of the four observations not reported in Yaqoob & Padmanabhan (2004) has a significant detection of narrow Fe  $K\alpha$  line, and that

contour has already been shown in Fig. 1.

**Figure 3**

Distributions of Fe  $K\alpha$  line core centroid energies constructed in four different ways. (a) and (b) were made using the results from individual observations, whereas (c) and (d) were made from measurements that used spectra averaged from multiple observations of a given source where relevant (see §4 for exceptions). In (a) and (c) the line intrinsic width was fixed at 1 eV (results from Table 1). In (b) and (d) the line centroid energies that could be measured with the line width free were utilized (i.e. those from Table 2), keeping the line measurements from Table 1 for the remainder. For the individual observations this results in 51 out of 68 values being obtained with the line width free –see text for details. The dashed and dotted lines in each case correspond to the distribution of 68% confidence lower and upper limits on the line centroid energy, respectively.

**Figure 4**

Distributions of Fe  $K\alpha$  line EW constructed in four different ways. (a) and (b) were made using the results from individual observations, whereas (c) and (d) were made from measurements that used spectra averaged from multiple observations of a given source where relevant (see §4 for exceptions). In (a) and (c) the line intrinsic width was fixed at 1 eV (results from Table 1). In (b) and (d) the line centroid energies that could be measured with the line width free were utilized (i.e. those from Table 2), keeping the line measurements from Table 1 for the remainder. For the individual observations this resulted in 70 out of 82 values being obtained with the line width free –see text for details. The dashed and dotted lines in each case correspond to the distribution of 68% confidence lower and upper limits on the line EW, respectively. The shaded histograms in both panels mark the 68% upper limits on the EW for 12 observations in which the EW could not be measured. Note that the largest EW of  $\sim 600$  eV (for PG 0844+349) is not shown in (b) and (d) because it is not a true measure of the narrow-line EW at  $\sim 6.4$  keV (see text).

**Figure 5**

The Fe  $K\alpha$  emission-line FWHM versus the  $H\beta$  FWHM for which the Fe  $K\alpha$  line width could be constrained (see text and Table 2). For MCG –5-23-16, we used the FWHM of infra-red broad  $Br\alpha$  line as a surrogate for  $H\beta$  FWHM. The dashed line corresponds to the two line widths being equal. Open circles correspond to the 12 cases shown in Fig. 6, for which the best Fe  $K\alpha$  line FWHM constraints were obtained (see text). The statistical errors on the Fe  $K\alpha$  line FWHM shown correspond to 68% confidence for three free parameters.

**Figure 6**

Joint 68%, 90%, and 99%, confidence contours of the Fe  $K\alpha$  emission-line core EW versus the ratio of the Fe  $K\alpha$  FWHM to the  $H\beta$  FWHM for 12 AGN that provided the best

measurements of Fe  $K\alpha$  line FWHM (see text). For MCG –5-23-16, we used the FWHM of infra-red broad Br $\alpha$  line as a surrogate for H $\beta$  FWHM. The vertical dotted lines correspond to a FWHM ratio of the pairs of emission lines equal to unity.

**Figure 7**

(a) The Fe  $K\alpha$  core emission-line EW versus the 2–10 keV luminosity. (b) As (a) for EW versus  $(L_{2-10 \text{ keV}}/L_{\text{Edd}})$ , a proxy for the accretion rate. Both (a) and (b) were constructed from measurements made from individual observations. (c) As (a) but showing EW versus  $L_{2-10 \text{ keV}}$  for measurements made from spectra combining multiple observations for a given source, where relevant. (d) As (c) but showing EW versus  $(L_{2-10 \text{ keV}}/L_{\text{Edd}})$ . In (c) and (d) the average spectrum was not used for all sources, for (b) and (d) reliable black-hole mass estimates were not available for all sources- see §4 and §5 for details. All of the measurements shown in (a)–(d) utilize results from the spectral fitting in which the Fe  $K\alpha$  line intrinsic width was fixed at 1 eV. The statistical errors on the Fe  $K\alpha$  line EW correspond to 68% confidence. The dotted lines show the correlations obtained by linear fits to  $\log$  EW versus  $\log L_{2-10 \text{ keV}}$  (a) and (c), and  $\log$  EW versus  $\log (L_{2-10 \text{ keV}}/L_{\text{Edd}})$  (b) and (d). Note that observations with only upper limits on the EW were not included in the fits.



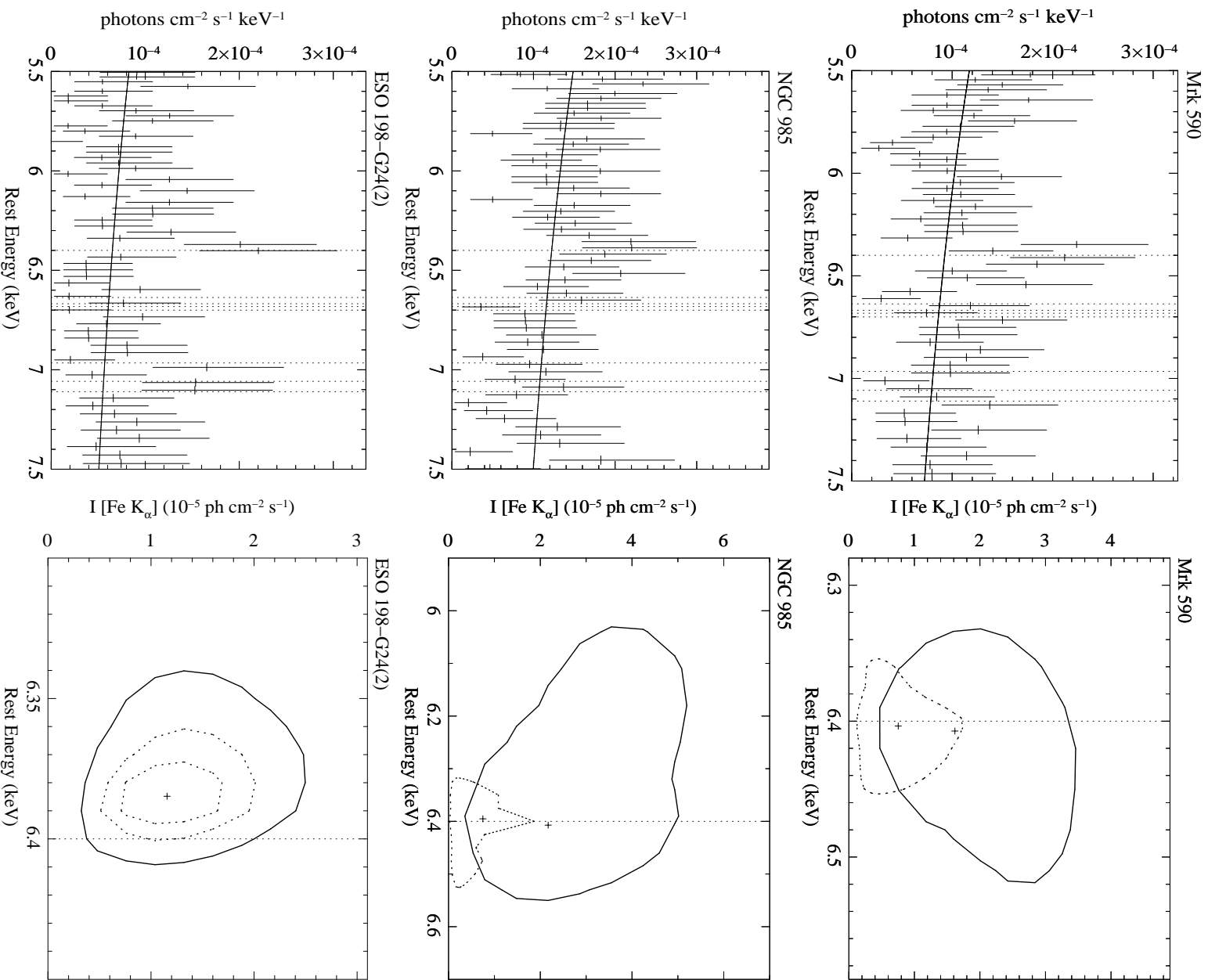


Fig. 1.—

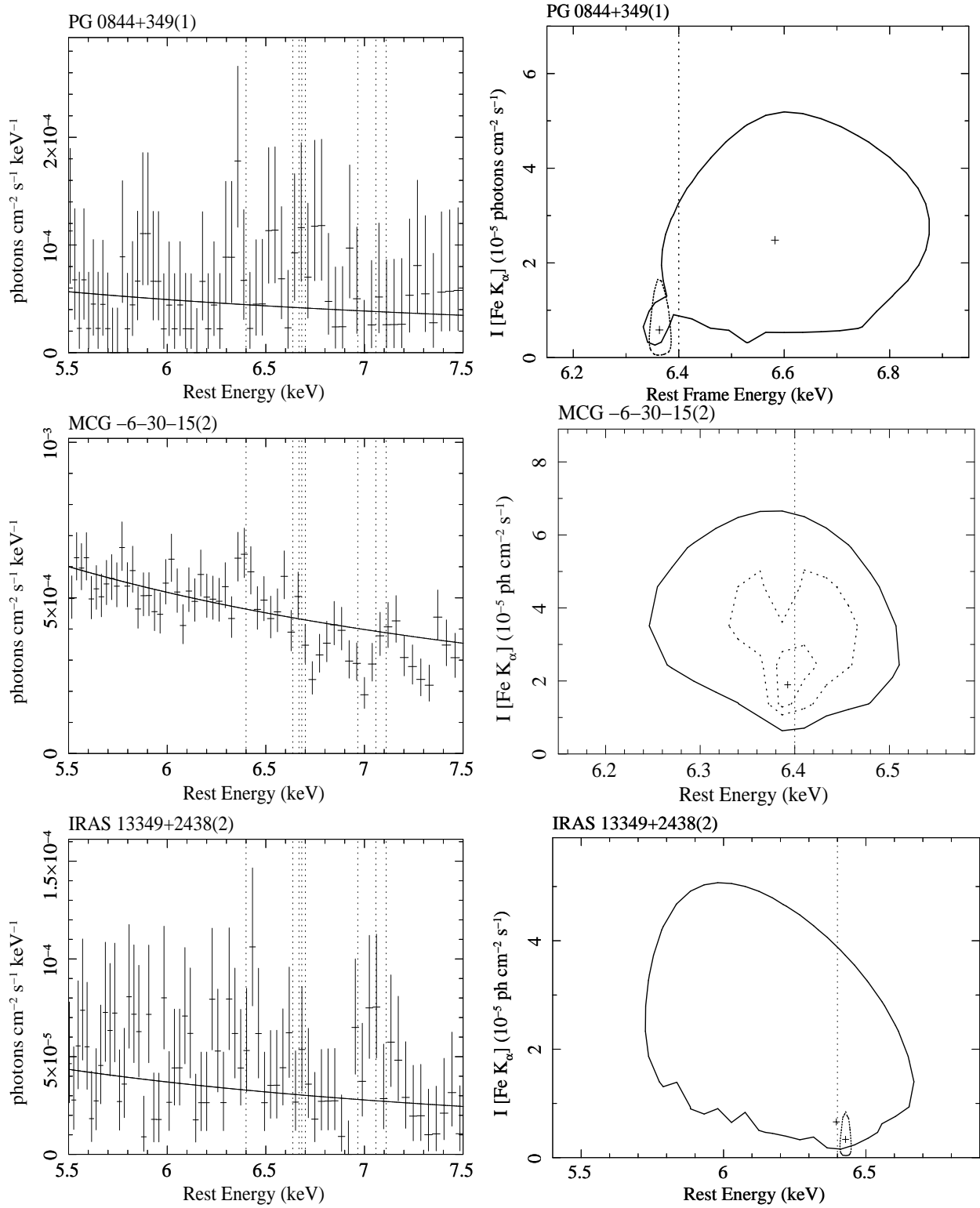


Fig. 1.— *continued*

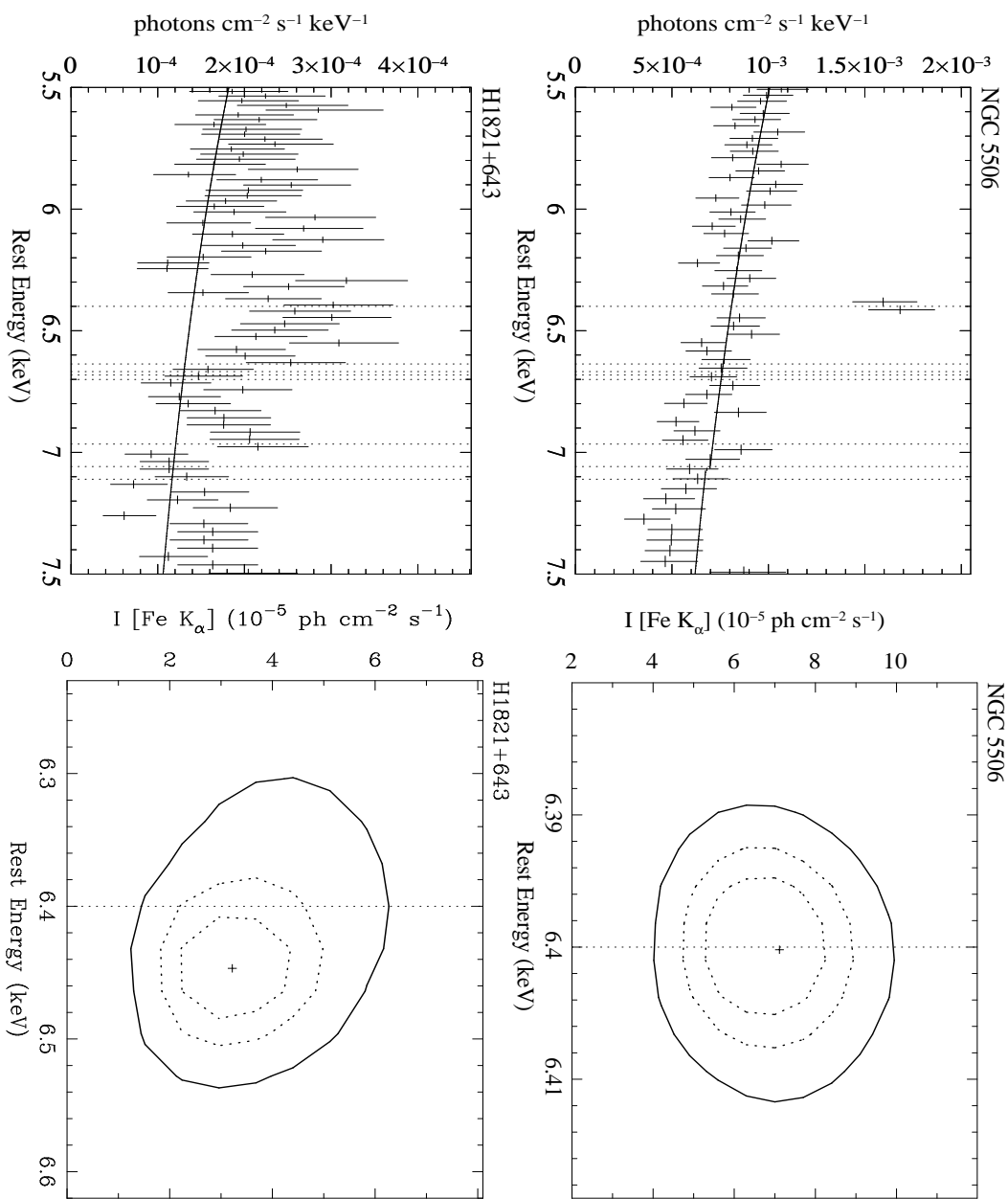


Fig. 1. — — *continued*

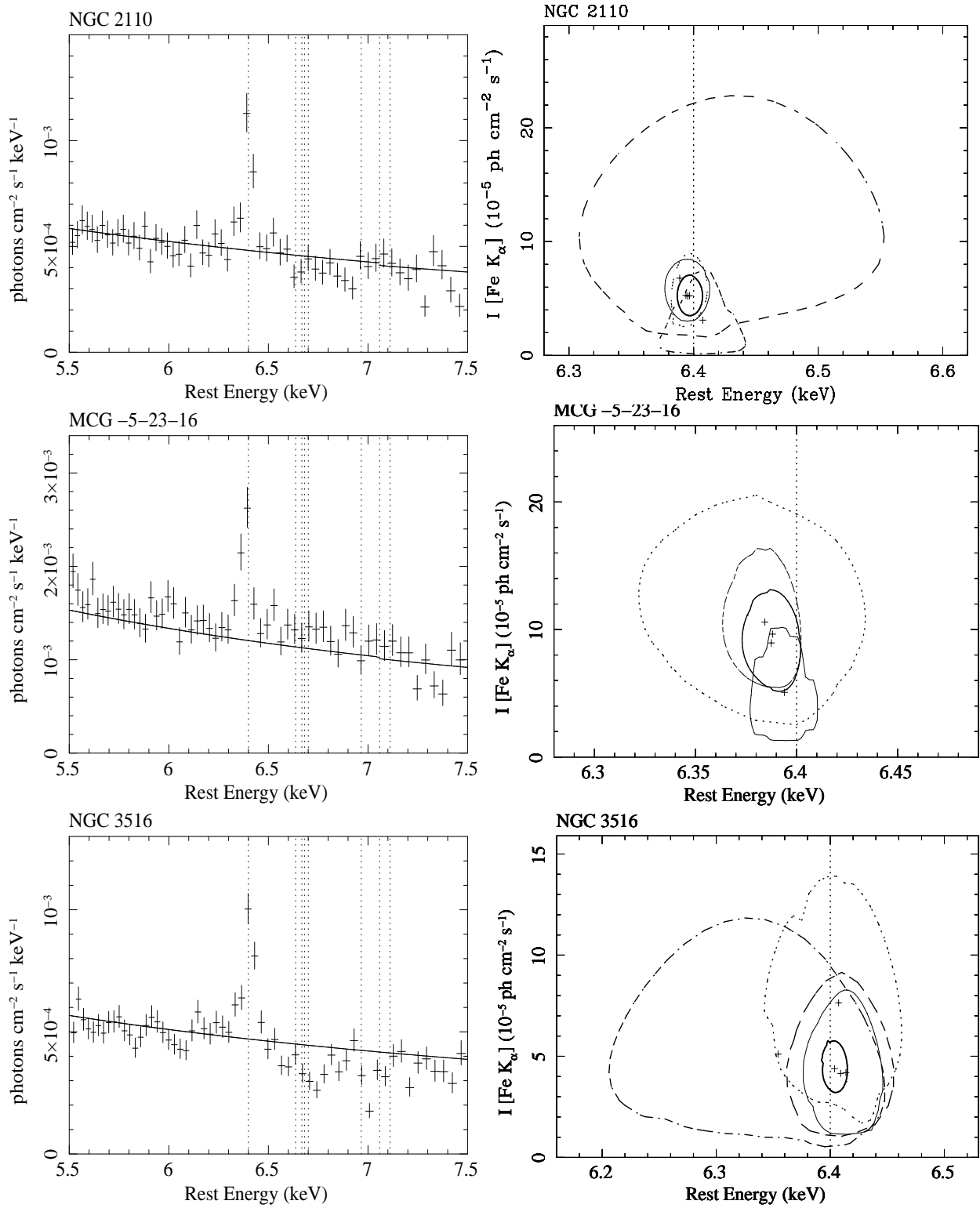


Fig. 2.—

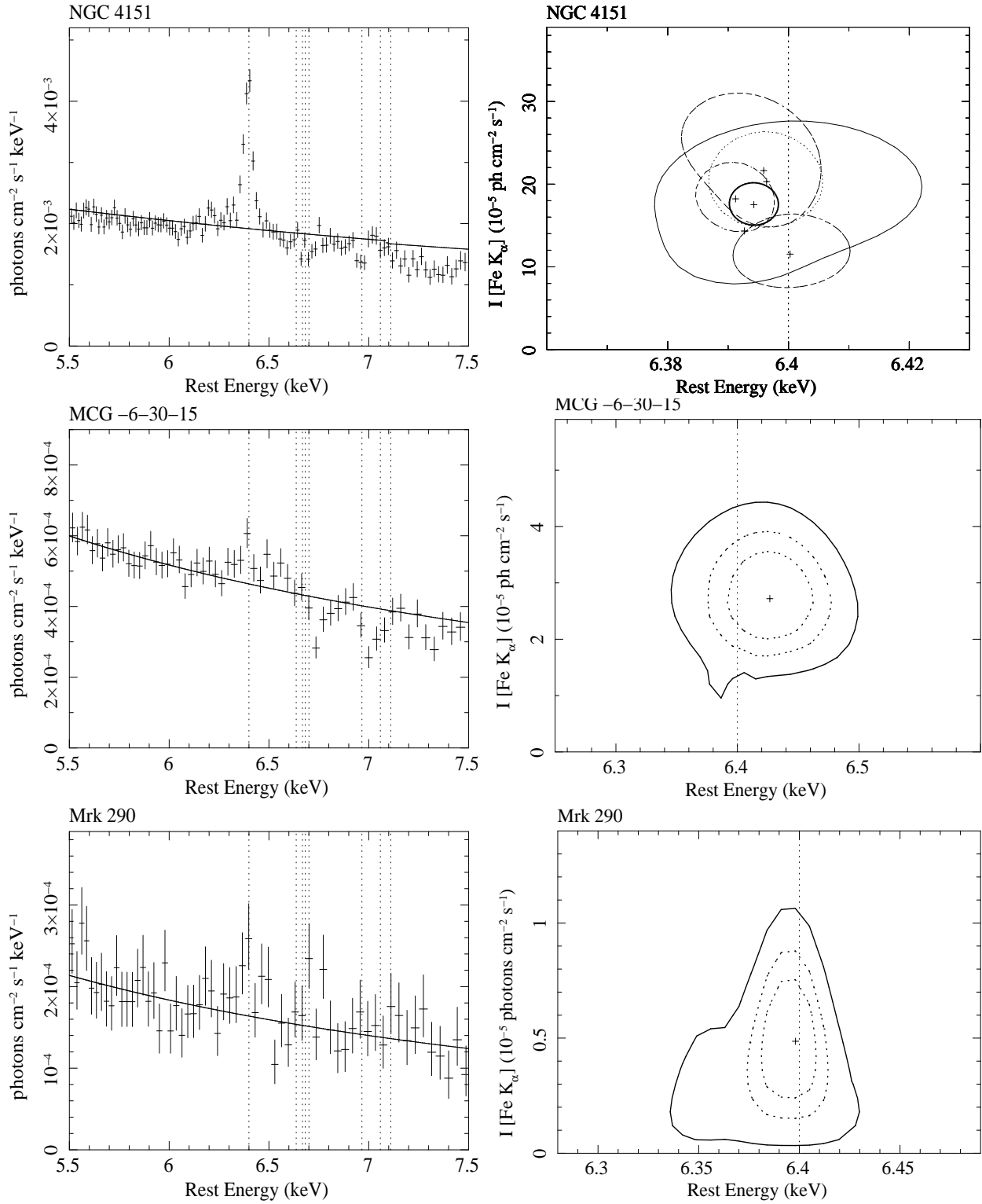


Fig. 2.— *continued*

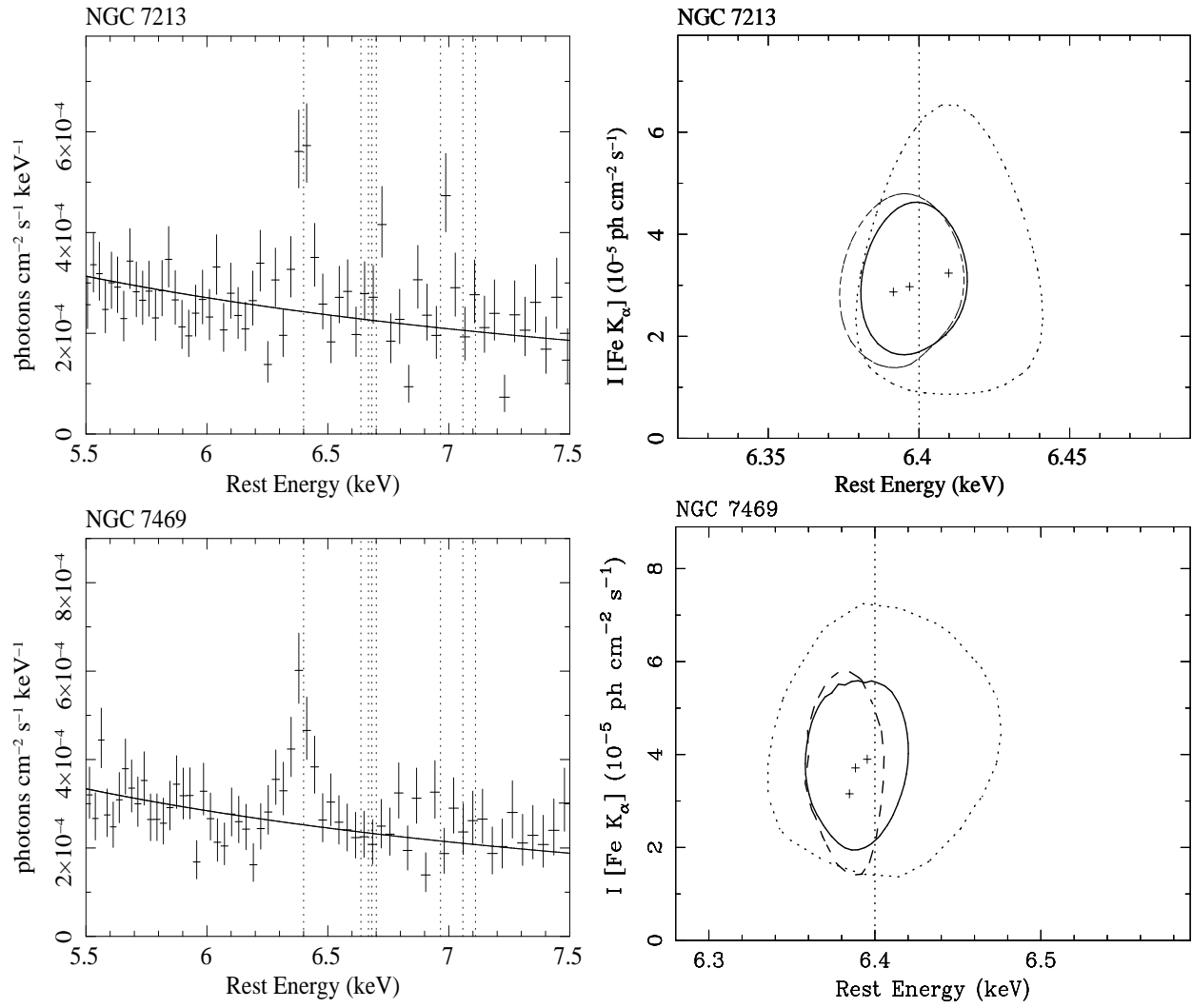


Fig. 2.— — *continued*

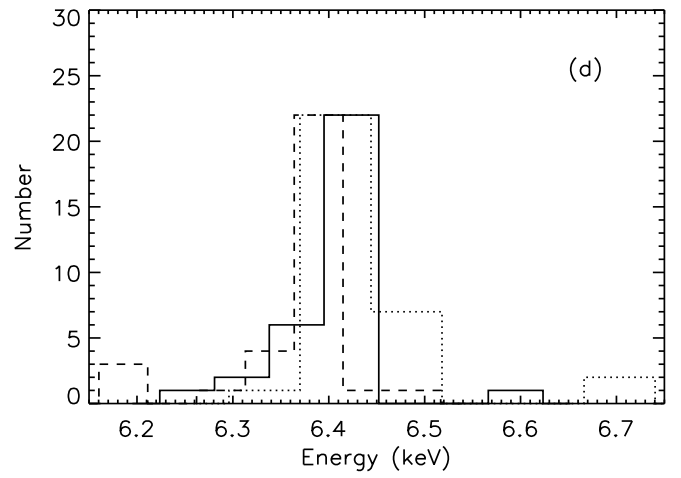
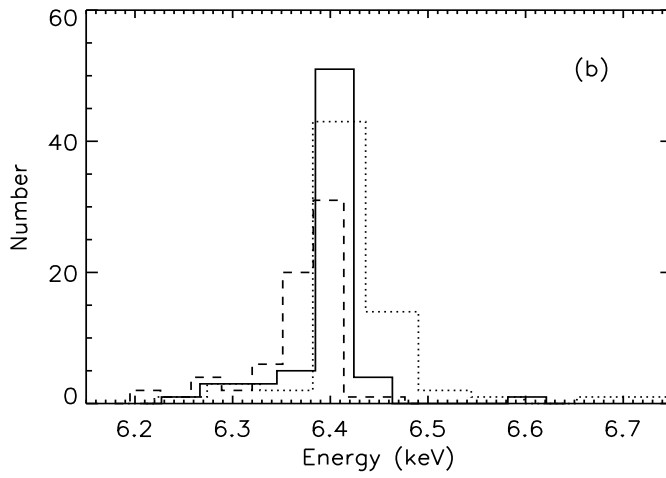
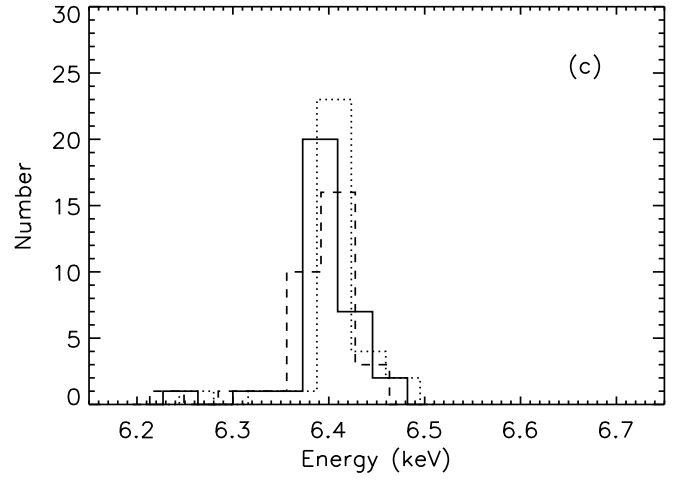
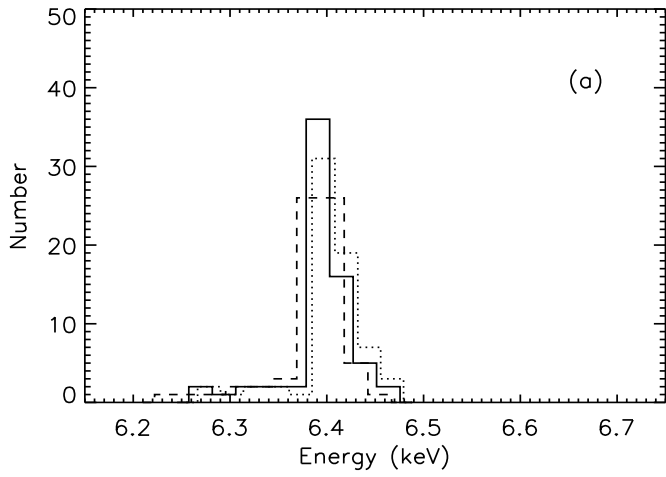


Fig. 3.—

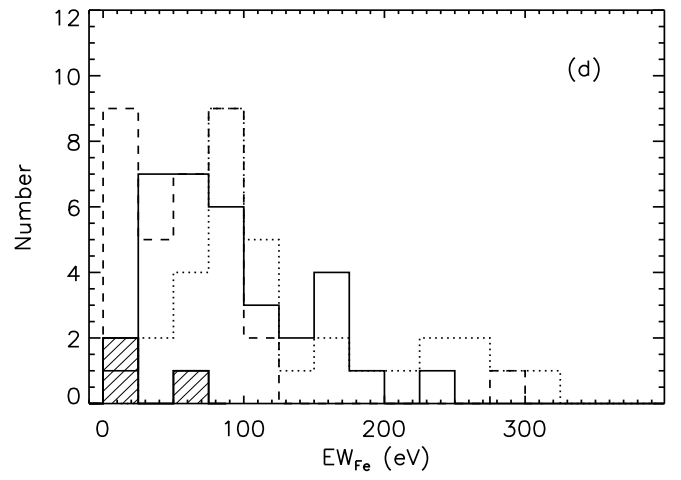
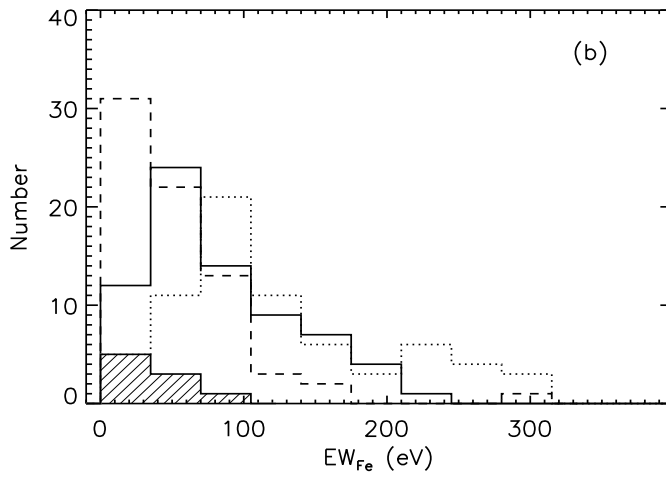
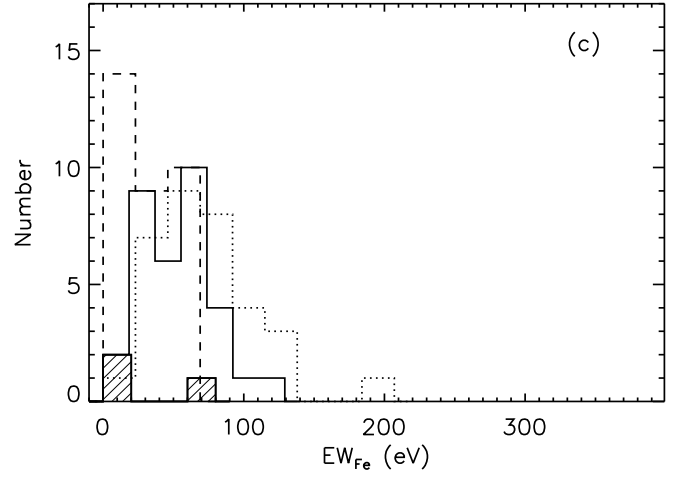
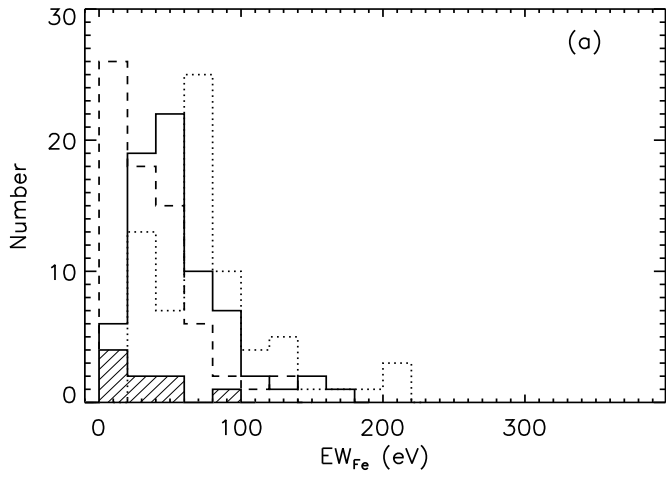


Fig. 4.—



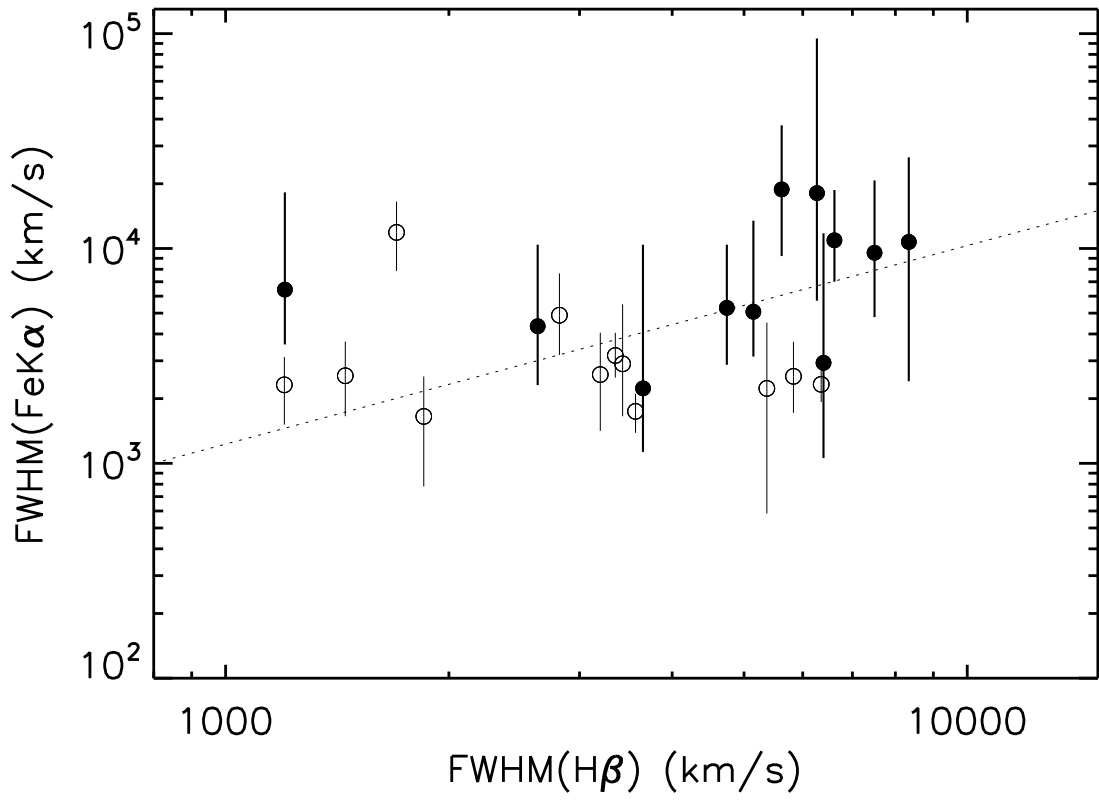


Fig. 5.—

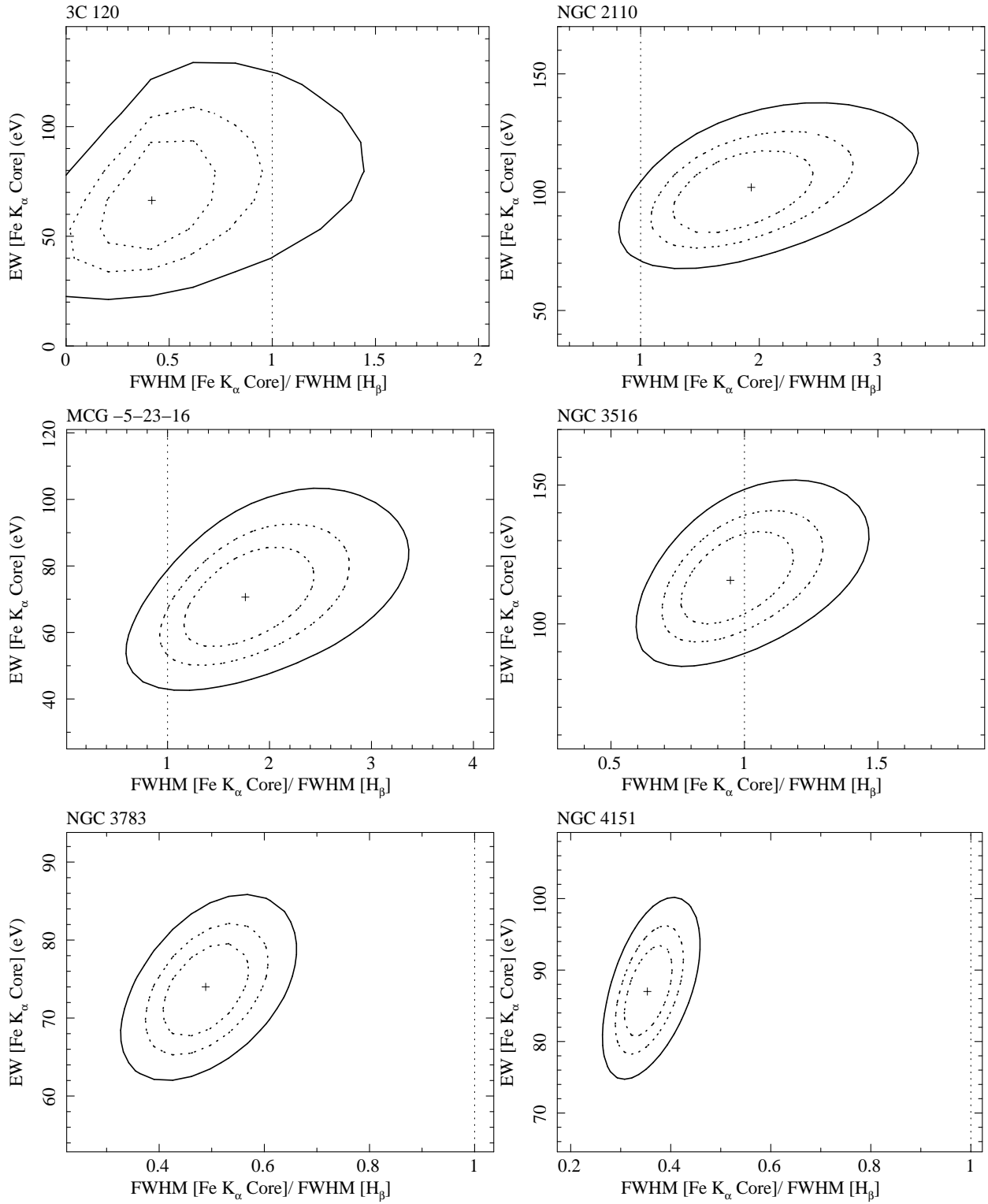


Fig. 6.—

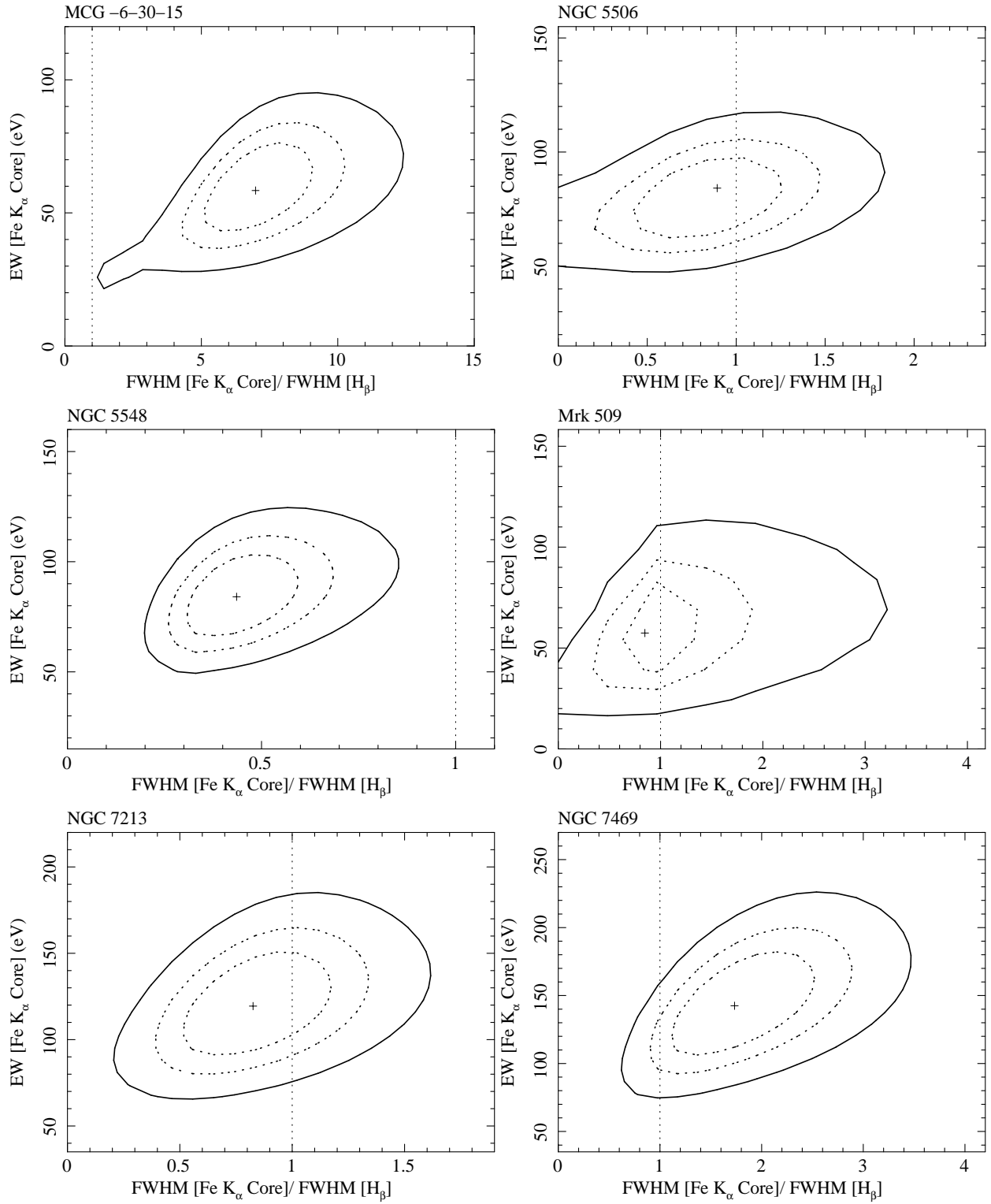


Fig. 6.— — *continued*

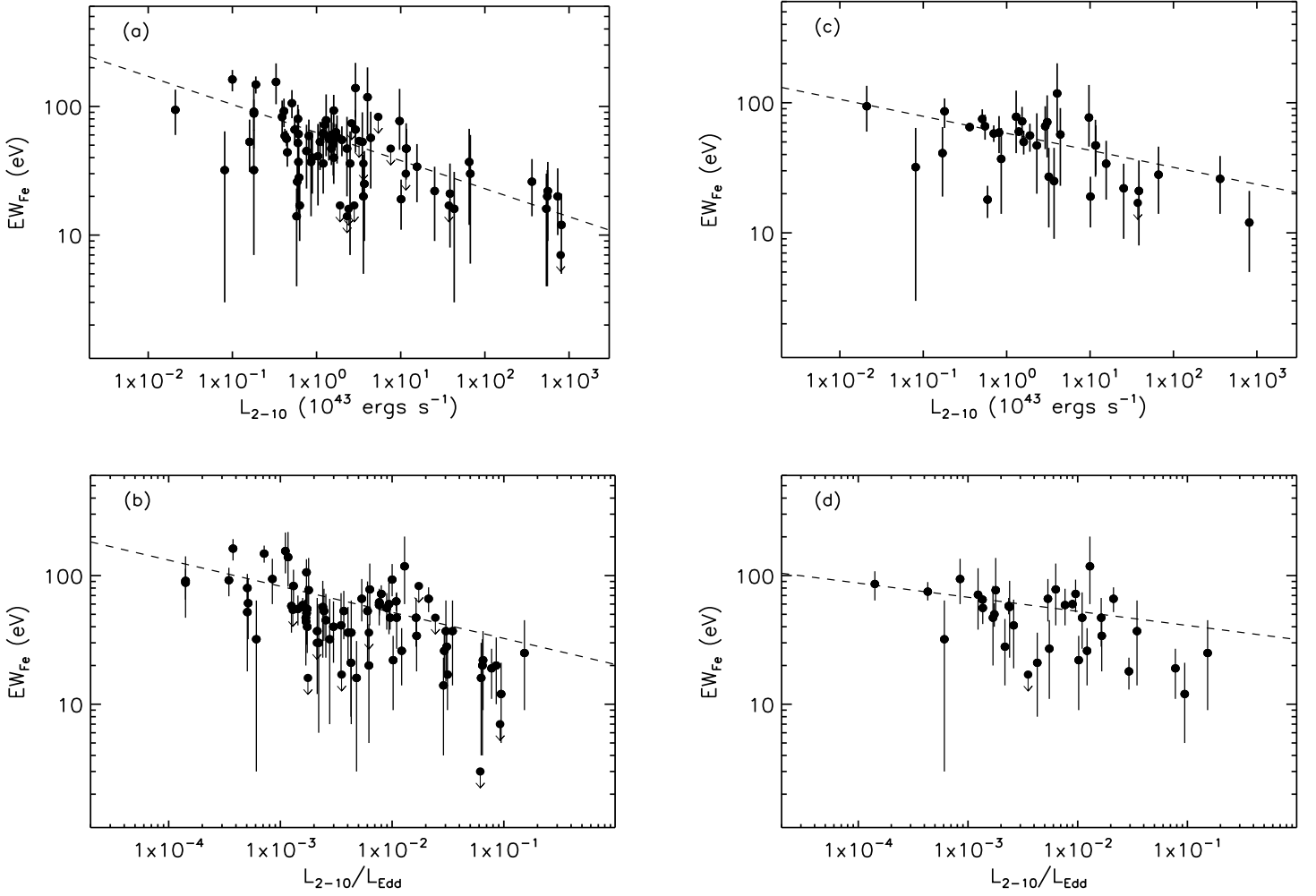


Fig. 7.— .

Table 1. PARAMETERS OF THE CORE FE K LINE EMISSION ( $\sigma=1$  eV) FROM *Chandra* (HEG) DATA

Source	$z$	Seq. Num /ObsID/exp	$E$ (keV)	$I$	$EW$ (eV)	$F$ (2–10 keV)	$L$ (2–10 keV)	$\Delta C$
(1)	(2)	(3)	(4)	(5)	(6)	(7)	(8)	(9)
Fairall 9	0.0470160	700278	$6.458^{+0.008}_{-0.016}$	$1.2^{+0.7}_{-0.5}$	$47^{+27}_{-20}$	2.2	11.6	14.4
		/2088/79.9	(6.434 – 6.468)	(0.5 – 2.2)	(20 – 86)			
NGC 526a(1)	0.0190970	700840	$6.400^f$	$0^{+0.6}_{-0}$	$0^{+16}_{-0}$	3.0	2.4	0
		/4376/29.1	...	(0 – 1.0)	(0 – 27)			
NGC 526a(2)	0.0190970	700840	$6.400^{+0.010}_{-0.006}$	$1.6^{+1.3}_{-0.9}$	$47^{+36}_{-27}$	3.0	2.3	8.0
		/4437/29.4	(6.389 – 6.413)	(0.3 – 3.5)	(9.0 – 100)			
NGC 526a(total)	0.0190970	...	$6.394^{+0.012}_{-0.006}$	$1.0^{+0.7}_{-0.7}$	$28^{+20}_{-20}$	2.9	2.4	5.0
		.../57.8	(6.380 – 6.414)	(0 – 2.1)	(0 – 59)			
Mrk 590	0.0263850	701005	$6.403^{+0.016}_{-0.009}$	$0.8^{+0.4}_{-0.4}$	$78^{+46}_{-37}$	0.85	1.3	14.9
		/4924/96.8	(6.386 – 6.435)	(0.3 – 1.5)	(31 – 155)			
NGC 985	0.0431430	700449	$6.395^{+0.015}_{-0.009}$	$0.7^{+0.5}_{-0.4}$	$57^{+34}_{-34}$	1.1	4.4	10.1
		/3010/77.7	(6.379 – 6.412)	(0.2 – 1.5)	(15 – 113)			
ESO 198–G24(1)	0.0455000	700900	$6.400^f$	$0.2^{+0.2}_{-0.2}$	$26^{+26}_{-26}$	0.67	3.2	1.6
		/4817/80.3	...	(0 – 0.6)	(0 – 74)			
ESO 198–G24(2)	0.0455000	700900	$6.386^{+0.008}_{-0.008}$	$1.0^{+0.6}_{-0.4}$	$139^{+79}_{-57}$	0.61	2.9	23.2
		/5315/71.5	(6.377 – 6.401)	(0.4 – 1.8)	(55 – 246)			
ESO 198–G24(total)	0.0455000	...	$6.394^{+0.008}_{-0.009}$	$0.6^{+0.3}_{-0.3}$	$71^{+43}_{-33}$	0.64	3.1	17.3
		.../151.5	(6.377 – 6.409)	(0.2 – 1.0)	(25 – 126)			
3C 120	0.00330100	700454	$6.412^{+0.009}_{-0.009}$	$2.5^{+1.1}_{-1.0}$	$47^{+20}_{-19}$	4.7	11.7	20.1
		/3015/58.2	(6.396 – 6.428)	(1.2 – 4.2)	(22 – 78)			
NGC 2110(1)	0.00778900	700582	$6.416^{+0.008}_{-0.010}$	$3.7^{+2.0}_{-1.8}$	$61^{+34}_{-29}$	4.5	0.61	14.1
		/3143/34	(6.397 – 6.430)	(1.3 – 6.8)	(22 – 113)			
NGC 2110(2)	0.00778900	700582	$6.407^{+0.015}_{-0.016}$	$3.1^{+2.5}_{-2.0}$	$52^{+41}_{-34}$	4.5	0.60	10.4
		/3417/33.2	(6.384 – 6.434)	(0.6 – 6.6)	(10 – 110)			
NGC 2110(3)	0.00778900	700582	$6.392^{+0.007}_{-0.002}$	$4.9^{+1.4}_{-1.3}$	$80^{+23}_{-21}$	4.5	0.60	51.5
		/3418/76.1	(6.384 – 6.400)	(3.1 – 7.0)	(51 – 114)			
NGC 2110(4)	0.00778900	700841	$6.392^{+0.008}_{-0.002}$	$3.9^{+0.9}_{-0.9}$	$92^{+23}_{-23}$	3.1	0.41	70.8
		/4377/96.4	(6.384 – 6.400)	(2.6 – 5.3)	(62 – 127)			
NGC 2110(total)	0.00778900	...	$6.399^{+0.001}_{-0.008}$	$3.9^{+0.7}_{-0.6}$	$75^{+14}_{-11}$	3.8	0.51	134
		.../200.4	(6.391 – 6.400)	(3.0 – 4.9)	(58 – 95)			
PG 0844+349(1)	0.0640000	701023	$6.364^{+0.007}_{-0.009}$	$0.6^{+0.4}_{-0.3}$	$118^{+83}_{-58}$	0.42	4.0	12.4
		/5599/57.2	(6.352 – 6.375)	(0.2 – 1.3)	(40 – 262)			
PG 0844+349(2)	0.0640000	701023	$6.400^f$	$0.2^{+0.3}_{-0.2}$	$36^{+47}_{-36}$	0.55	5.4	1.3
		/6244/50.2	...	(0 – 0.7)	(0 – 116)			
PG 0844+349(3)	0.0640000	701023	$6.400^f$	$0.1^{+0.3}_{-0.1}$	$13^{+34}_{-13}$	0.77	7.6	0.2
		/6245/36.2	...	(0 – 0.6)	(0 – 76)			
PG 0844+349(total)	0.0640000	...	$6.366^{+0.008}_{-0.008}$	$0.3^{+0.3}_{-0.1}$	$52^{+43}_{-20}$	0.55	5.4	10.2
		.../141.2	(6.356 – 6.381)	(0.1 – 0.7)	(16 – 112)			
Mrk 705	0.0291500	700995	$6.400^f$	$0.4^{+0.6}_{-0.4}$	$26^{+48}_{-26}$	1.3	2.6	0.5
		/4914/21.3	...	(0 – 1.6)	(0 – 113)			
MCG –5-23-16(1)	0.00827900	700311	$6.394^{+0.007}_{-0.007}$	$7.2^{+2.1}_{-1.9}$	$55^{+18}_{-14}$	10.5	1.6	47
		/2121/76.2	(6.386 – 6.402)	(4.6 – 10)	(35 – 81)			
MCG –5-23-16(2)	0.00827900	701171	$6.394^{+0.008}_{-0.008}$	$5.1^{+2.5}_{-2.0}$	$40^{+20}_{-15}$	10.6	1.6	18.3
		/6187/30.1	(6.384 – 6.403)	(2.3 – 8.6)	(18 – 68)			

Table 1—Continued

Source	$z$	Seq. Num /ObsID/exp	$E$ (keV)	$I$	$EW$ (eV)	$F$ (2–10 keV)	$L$ (2–10 keV)	$\Delta C$
(1)	(2)	(3)	(4)	(5)	(6)	(7)	(8)	(9)
MCG –5-23-16(3)	0.00827900	701171	$6.395^{+0.015}_{-0.010}$	$6.4^{+3.0}_{-2.8}$	$51^{+24}_{-22}$	10.5	1.6	16.7
		/7240/20.3	(6.371 – 6.411)	(2.6 – 10)	(21 – 87)			
MCG –5-23-16(total)	0.00827900	...	$6.394^{+0.002}_{-0.001}$	$6.4^{+1.4}_{-1.3}$	$50^{+11}_{-10}$	10.5	1.6	80.9
		.../96.1	(6.387 – 6.402)	(4.6 – 8.4)	(36 – 65)			
NGC 3227	0.00385900	700165	$6.388^{+0.021}_{-0.012}$	$1.0^{+1.0}_{-0.9}$	$32^{+32}_{-29}$	2.5	0.08	3.1
		/860/47	...	(0 – 2.6)	(0 – 83)			
NGC 3516(1)	0.00883600	700270	$6.395^{+0.002}_{-0.006}$	$3.8^{+1.0}_{-0.9}$	$106^{+28}_{-25}$	3.0	0.51	69.3
		/2080/74.5	(6.383 – 6.398)	(2.5 – 5.2)	(70 – 145)			
NGC 3516(2)	0.00883600	700270	$6.406^{+0.009}_{-0.008}$	$3.7^{+1.5}_{-1.2}$	$155^{+61}_{-51}$	1.9	0.33	38.2
		/2431/36.2	(6.397 – 6.416)	(2.1 – 5.9)	(87 – 246)			
NGC 3516(3)	0.00883600	700270	$6.398^{+0.002}_{-0.008}$	$2.4^{+0.9}_{-0.7}$	$83^{+28}_{-26}$	2.3	0.39	40.6
		/2482/89.5	(6.389 – 6.407)	(1.4 – 3.6)	(47 – 121)			
NGC 3516(4)	0.00883600	701337	$6.407^{+0.016}_{-0.010}$	$2.5^{+1.4}_{-1.2}$	$40^{+23}_{-19}$	5.2	0.89	12.5
		/7281/43.1	(6.373 – 6.430)	(0.8 – 4.6)	(13 – 74)			
NGC 3516(5)	0.00883600	701337	$6.398^{+0.009}_{-0.008}$	$2.3^{+1.4}_{-1.1}$	$45^{+27}_{-22}$	4.4	0.76	12.9
		/7282/42.1	(6.383 – 6.414)	(0.8 – 4.3)	(16 – 83)			
NGC 3516(6)	0.00883600	701337	$6.430^{+0.008}_{-0.008}$	$3.8^{+1.6}_{-1.5}$	$53^{+23}_{-21}$	6.5	1.1	20.6
		/8450/39.1	(6.415 – 6.439)	(1.7 – 6.2)	(24 – 87)			
NGC 3516(7)	0.00883600	701337	$6.407^{+0.030}_{-0.010}$	$2.7^{+1.6}_{-1.1}$	$36^{+21}_{-15}$	6.7	1.2	14.4
		/8451/48.1	(6.389 – 6.439)	(1.1 – 4.9)	(15 – 65)			
NGC 3516(8)	0.00883600	701337	$6.431^{+0.009}_{-0.033}$	$2.9^{+2.2}_{-1.8}$	$41^{+32}_{-24}$	6.1	1.0	7.2
		/8452/20.2	(6.390 – 6.447)	(0.5 – 6.2)	(7.0 – 88)			
NGC 3516(total)	0.00883600	...	$6.398^{+0.001}_{-0.001}$	$2.8^{+0.4}_{-0.4}$	$58^{+9}_{-8}$	4.1	0.70	161.7
		.../386.5	(6.397 – 6.400)	(2.2 – 3.4)	(46 – 71)			
NGC 3783(1)	0.00973000	700045	$6.396^{+0.007}_{-0.008}$	$4.4^{+1.3}_{-1.4}$	$56^{+17}_{-18}$	6.8	1.4	36.6
		/373/57.2	(6.387 – 6.404)	(2.5 – 6.4)	(32 – 88)			
NGC 3783(2)	0.00973000	700280	$6.403^{+0.001}_{-0.008}$	$4.2^{+0.8}_{-0.8}$	$61^{+11}_{-12}$	5.9	1.2	105.2
		/2090/167.8	(6.395 – 6.404)	(3.1 – 5.4)	(45 – 78)			
NGC 3783(3)	0.00973000	700281	$6.395^{+0.001}_{-0.001}$	$4.3^{+0.8}_{-0.8}$	$62^{+12}_{-11}$	5.9	1.2	109.2
		/2091/171	(6.387 – 6.397)	(3.2 – 5.5)	(46 – 79)			
NGC 3783(4)	0.00973000	700282	$6.396^{+0.001}_{-0.001}$	$5.0^{+0.8}_{-0.8}$	$72^{+12}_{-11}$	6.0	1.3	146.6
		/2092/167.6	(6.394 – 6.401)	(3.9 – 6.2)	(56 – 90)			
NGC 3783(5)	0.00973000	700283	$6.396^{+0.001}_{-0.001}$	$5.8^{+0.9}_{-0.9}$	$63^{+10}_{-10}$	8.2	1.7	154.2
		/2093/168.2	(6.394 – 6.397)	(4.5 – 7.1)	(49 – 77)			
NGC 3783(6)	0.00973000	700284	$6.396^{+0.008}_{-0.001}$	$4.0^{+0.8}_{-0.8}$	$48^{+10}_{-9}$	7.2	1.5	89.3
		/2094/168.3	(6.394 – 6.404)	(2.9 – 5.2)	(35 – 62)			
NGC 3783(total)	0.00973000	...	$6.396^{+0.001}_{-0.001}$	$4.6^{+0.4}_{-0.3}$	$60^{+5}_{-4}$	6.6	1.4	635.9
		.../888.7	(6.395 – 6.396)	(4.1 – 5.1)	(53 – 66)			
NGC 4051	0.00233600	700164	$6.414^{+0.006}_{-0.010}$	$1.6^{+0.9}_{-0.5}$	$94^{+41}_{-34}$	1.7	0.02	26.5
		/859/80.8	(6.398 – 6.422)	(0.9 – 2.8)	(49 – 152)			
NGC 4151(1)	0.00331900	700007	$6.396^{+0.001}_{-0.001}$	$17.2^{+2.7}_{-2.6}$	$148^{+23}_{-22}$	7.8	0.19	202.3
		/335/48	(6.395 – 6.398)	(13 – 21)	(117 – 182)			
NGC 4151(2)	0.00331900	700491	$6.396^{+0.001}_{-0.001}$	$13.9^{+1.6}_{-1.4}$	$59^{+8}_{-6}$	17.4	0.42	306.5
		/3052/156.6	(6.394 – 6.396)	(11 – 16)	(50 – 69)			

Table 1—Continued

Source	$z$	Seq. Num /ObsID/exp	$E$ (keV)	$I$	$EW$ (eV)	$F$ (2–10 keV)	$L$ (2–10 keV)	$\Delta C$
(1)	(2)	(3)	(4)	(5)	(6)	(7)	(8)	(9)
NGC 4151(3)	0.00331900	700491 /3480/92.9	$6.396^{+0.001}_{-0.001}$ (6.394 – 6.397)	$14.0^{+2.1}_{-1.9}$ (11 – 17)	$56^{+9}_{-7}$ (46 – 69)	18.3	0.44	177.1
NGC 4151(4)	0.00331900	701493 /7829/50	$6.396^{+0.008}_{-0.001}$ (6.395 – 6.404)	$10.0^{+1.8}_{-2.0}$ (7.4 – 12)	$162^{+30}_{-31}$ (119 – 206)	4.3	0.10	131.1
NGC 4151(5)	0.00331900	701494 /7830/50.2	$6.388^{+0.008}_{-0.001}$ (6.386 – 6.397)	$11.1^{+2.6}_{-2.5}$ (7.6 – 14)	$44^{+10}_{-10}$ (30 – 59)	18.4	0.45	63.4
NGC 4151(total)	0.00331900	... .../389.9	$6.396^{+0.001}_{-0.001}$ (6.395 – 6.396)	$13.3^{+0.9}_{-0.9}$ (12 – 14)	$65^{+5}_{-4}$ (59 – 72)	14.9	0.36	801.5
Mrk 766	0.0129290	700123 /1597/90.5	$6.425^{+0.016}_{-0.010}$ (6.400 – 6.450)	$0.8^{+0.6}_{-0.5}$ (0.2 – 1.6)	$37^{+27}_{-23}$ (9.0 – 73)	2.3	0.86	7.9
3C 273(1)	0.158340	790020 /459/39.1	$6.313^{+0.013}_{-0.015}$ (6.291 – 6.334)	$2.4^{+1.7}_{-1.5}$ (0.4 – 4.8)	$12^{+9}_{-7}$ (2.0 – 24)	12.4	811.4	6.7
3C 273(2)	0.158340	790057 /2463/27.1	$6.292^{+0.007}_{-0.007}$ (6.279 – 6.301)	$3.2^{+1.9}_{-1.7}$ (0.8 – 6.0)	$20^{+13}_{-10}$ (5.0 – 38)	11.2	734	9.25
3C 273(3)	0.158340	790074 /3456/25	$6.275^{+0.011}_{-0.010}$ (6.259 – 6.293)	$2.5^{+1.8}_{-1.5}$ (0.4 – 5.2)	$22^{+15}_{-13}$ (3.0 – 45)	8.4	559	7.2
3C 273(4)	0.158340	790075 /3457/25.4	$6.319^{+0.008}_{-0.012}$ ...	$2.2^{+1.4}_{-1.7}$ (0.0 – 4.4)	$20^{+12}_{-16}$ (0.0 – 39)	8.3	552	4.3
3C 273(5)	0.158340	790076 /3573/30.2	$6.412^{+0.021}_{-0.029}$ ...	$1.7^{+1.6}_{-1.3}$ (0.0 – 4.1)	$16^{+14}_{-12}$ (0.0 – 38)	8.1	538	4.0
3C 273(6)	0.158340	790087 /4430/27.6	$6.400^f$ ...	$0^{+0.9}_{-0}$ (0.0 – 1.6)	$0^{+7}_{-0}$ (0.0 – 10)	11.9	794	0
3C 273(7)	0.158340	790089 /5169/30.2	$6.400^f$ ...	$0.0^{+0.4}_{-0.0}$ (0.0 – 0.9)	$0^{+3}_{-0}$ (0.0 – 7.0)	8.0	528	2.0
3C 273(total)	0.158340	... .../201.1	$6.319^{+0.007}_{-0.013}$ (6.292 – 6.328)	$1.0^{+0.6}_{-0.6}$ (0.2 – 1.8)	$7^{+4}_{-4}$ (1.0 – 13)	9.9	654	8.0
NGC 4593	0.00900000	700279 /2089/79.9	$6.399^{+0.008}_{-0.008}$ (6.390 – 6.408)	$2.7^{+1.0}_{-0.8}$ (1.6 – 4.1)	$59^{+20}_{-18}$ (34 – 88)	4.5	0.81	33.3
MCG –6-30-15(1)	0.00774900	700105 /433/128.2	$6.384^{+0.015}_{-0.009}$ (6.374 – 6.407)	$1.4^{+0.6}_{-0.6}$ (0.6 – 2.3)	$28^{+12}_{-12}$ (12 – 46)	4.7	0.62	15.9
MCG –6-30-15(2)	0.00774900	700845 /4759/161.1	$6.399^{+0.008}_{-0.008}$ (6.389 – 6.409)	$1.2^{+0.6}_{-0.4}$ (0.6 – 2.1)	$26^{+12}_{-9}$ (17 – 44)	4.5	0.59	17.4
MCG –6-30-15(3)	0.00774900	700845 /4760/172.3	$6.382^{+0.009}_{-0.013}$ (6.359 – 6.400)	$0.7^{+0.4}_{-0.5}$ (0.0 – 1.3)	$14^{+9}_{-10}$ (0 – 27)	4.4	0.58	5.5
MCG –6-30-15(4)	0.00774900	700845 /4761/158.8	$6.400^{+0.016}_{-0.018}$ (6.375 – 6.424)	$0.8^{+0.6}_{-0.4}$ (0.2 – 1.7)	$17^{+11}_{-8}$ (4.0 – 33)	4.7	0.63	7.4
MCG –6-30-15(5)	0.00774900	700845 /4762/38.2	$6.342^{+0.018}_{-0.021}$ (6.312 – 6.368)	$1.8^{+1.3}_{-1.1}$ (0.3 – 3.7)	$37^{+27}_{-22}$ (6.0 – 77)	4.6	0.61	7.6
MCG –6-30-15(total)	0.00774900	... .../582	$6.390^{+0.002}_{-0.008}$ (6.375 – 6.399)	$0.8^{+0.3}_{-0.2}$ (0.5 – 1.2)	$18^{+5}_{-5}$ (10 – 25)	4.5	0.59	29.1
IRAS 13349+2438(1)	0.107640	700902 /4819/161.9	$6.400^f$ ...	$0.04^{+0.1}_{-0.04}$ (0.0 – 0.2)	$8^{+22}_{-8}$ (0.0 – 46)	0.39	11.5	0.3
IRAS 13349+2438(2)	0.107640	700902 /4820/137.5	$6.428^{+0.011}_{-0.008}$ (6.417 – 6.440)	$0.3^{+0.3}_{-0.1}$ (0.1 – 0.7)	$77^{+60}_{-31}$ (23 – 160)	0.33	9.7	12.9

Table 1—Continued

Source	$z$	Seq. Num /ObsID/exp	$E$ (keV)	$I$	$EW$ (eV)	$F$ (2–10 keV)	$L$ (2–10 keV)	$\Delta C$
(1)	(2)	(3)	(4)	(5)	(6)	(7)	(8)	(9)
IRAS 13349+2438(total)	0.107640	...	$6.426^{+0.013}_{-0.009}$	$0.2^{+0.1}_{-0.1}$	$40^{+22}_{-19}$	0.36	10.7	9.7
		.../294.5	(6.411 – 6.441)	(0.0 – 0.4)	(0.0 – 83)			
IC 4329A	0.0160540	700367	$6.399^{+0.006}_{-0.005}$	$3.7^{+1.6}_{-1.6}$	$19^{+8}_{-8}$	17.5	10.1	14.3
		/2177/60.1	(6.387 – 6.411)	(1.5 – 6.1)	(8.0 – 31)			
Mrk 279	0.0304510	700501	$6.381^{+0.008}_{-0.007}$	$1.1^{+0.4}_{-0.4}$	$66^{+28}_{-22}$	1.4	2.9	23.4
		/3062/116.1	(6.372 – 6.395)	(0.5 – 1.7)	(31 – 107)			
NGC 5506	0.00618100	700214	$6.398^{+0.008}_{-0.001}$	$5.7^{+1.3}_{-1.2}$	$66^{+15}_{-14}$	6.6	0.55	80.6
		/1598/90	(6.396 – 6.406)	(4.1 – 7.6)	(48 – 88)			
NGC 5548(1)	0.0171750	700142	$6.410^{+0.016}_{-0.009}$	$1.8^{+0.8}_{-0.7}$	$58^{+27}_{-22}$	2.7	1.8	22.1
		/837/82.3	(6.385 – 6.434)	(0.9 – 3.0)	(29 – 98)			
NGC 5548(2)	0.0171750	700485	$6.394^{+0.008}_{-0.007}$	$1.9^{+0.5}_{-0.5}$	$55^{+15}_{-14}$	3.1	2.0	42.2
		/3046/153.9	(6.386 – 6.403)	(1.2 – 2.7)	(35 – 78)			
NGC 5548(total)	0.0171750	...	$6.402^{+0.001}_{-0.010}$	$1.9^{+0.4}_{-0.5}$	$56^{+13}_{-14}$	2.9	1.9	61.8
		.../232.7	(6.386 – 6.410)	(1.3 – 2.5)	(39 – 75)			
Mrk 290(1)	0.0295770	700629	$6.386^{+0.012}_{-0.011}$	$1.0^{+0.7}_{-0.6}$	$53^{+37}_{-32}$	1.8	3.5	9.0
		/3567/55.1	(6.367 – 6.400)	(0.2 – 2.0)	(11 – 106)			
Mrk 290(2)	0.0295770	700629	$6.398^{+0.026}_{-0.032}$	$0.5^{+0.4}_{-0.4}$	$36^{+28}_{-29}$	1.3	2.5	3.8
		/4399/85.1	...	(0 – 1.2)	(0 – 85)			
Mrk 290(3)	0.0295770	700629	$6.400^f$	$0.4^{+0.4}_{-0.3}$	$20^{+22}_{-15}$	1.8	3.6	1.8
		/4441/60.9	...	(0 – 1.0)	(0 – 52)			
Mrk 290(4)	0.0295770	700629	$6.400^f$	$0.3^{+0.4}_{-0.3}$	$15^{+21}_{-15}$	1.8	3.6	0.8
		/4442/50.2	...	(0 – 1.0)	(0 – 51)			
Mrk 290(total)	0.0295770	...	$6.398^{+0.009}_{-0.016}$	$0.5^{+0.3}_{-0.3}$	$27^{+18}_{-16}$	1.6	3.2	10.8
		.../247.3	(6.374 – 6.414)	(0.2 – 0.9)	(11 – 50)			
PDS 456	0.184000	700742	$6.400^f$	$0.04^{+0.06}_{-0.04}$	$4^{+13}_{-4}$	0.40	37.3	0.11
		/4063/145.2	...	(0 – 0.2)	(0 – 33)			
E1821+643	0.297000	700215	$6.453^{+0.005}_{-0.007}$	$0.7^{+0.4}_{-0.3}$	$26^{+13}_{-12}$	1.4	362.5	13.1
		/1599/101.3	(6.445 – 6.463)	(0.3 – 1.3)	(11 – 46)			
3C 382(1)	0.0578700	700991	$6.374^{+0.017}_{-0.016}$	$1.0^{+1.0}_{-0.8}$	$16^{+15}_{-13}$	5.5	43.2	3.7
		/4910/55	...	(0 – 2.5)	(0 – 39)			
3C 382(2)	0.0578700	700991	$6.408^{+0.013}_{-0.010}$	$1.3^{+0.9}_{-0.8}$	$21^{+15}_{-13}$	4.9	38.5	7.1
		/6151/64.9	(6.382 – 6.429)	(0.2 – 2.6)	(3.0 – 43)			
3C 382(total)	0.0578700	...	$6.368^{+0.038}_{-0.009}$	$0.9^{+0.6}_{-0.6}$	$14^{+9}_{-9}$	5.2	40.6	6.2
		.../118	(6.351 – 6.446)	(0.1 – 1.8)	(2.0 – 28)			
IRAS 18325–5926(1)	0.0202310	700587	$6.400^f$	$0.05^{+0.35}_{-0.05}$	$2^{+15}_{-2}$	2.1	1.9	0.04
		/3148/56.9	...	(0 – 0.7)	(0.0 – 31)			
IRAS 18325–5926(2)	0.0202310	700587	$6.400^f$	$0.2^{+0.4}_{-0.2}$	$5^{+12}_{-5}$	3.1	2.8	0.2
		/3452/51.1	...	(0 – 1.0)	(0.0 – 29)			
IRAS 18325–5926(total)	0.0202310	...	$6.400^f$	$0.1^{+0.3}_{-0.1}$	$5^{+9}_{-5}$	2.5	2.3	0.2
		.../106.2	...	(0 – 0.6)	(0 – 21)			
4C +74.26(1)	0.104000	700679	$6.258^{+0.013}_{-0.014}$	$1.2^{+1.0}_{-0.8}$	$37^{+30}_{-25}$	2.5	65.1	6.8
		/4000/37.7	(6.236 – 6.278)	(0.2 – 2.6)	(6.0 – 79)			
4C +74.26(2)	0.104000	700679	$6.347^{+0.011}_{-0.010}$	$1.0^{+1.0}_{-0.8}$	$30^{+30}_{-24}$	2.6	67.1	4.7
		/5195/31.8	(6.322 – 6.366)	(0.0 – 2.4)	(0.0 – 73)			



Table 1—Continued

Source	$z$	Seq. Num /ObsID/exp	$E$ (keV)	$I$	$EW$ (eV)	$F$ (2–10 keV)	$L$ (2–10 keV)	$\Delta C$
(1)	(2)	(3)	(4)	(5)	(6)	(7)	(8)	(9)
4C +74.26(total)	0.104000	...	$6.252^{+0.011}_{-0.008}$	$1.0^{+0.7}_{-0.5}$	$28^{+18}_{-14}$	2.5	66.2	9.5
		.../66.1	(6.242 – 6.265)	(0.3 – 2.0)	(8.0 – 54)			
Mrk 509	0.0343970	700277	$6.445^{+0.015}_{-0.009}$	$2.2^{+1.2}_{-1.0}$	$34^{+17}_{-16}$	5.8	15.6	13.7
		/2087/58.7	(6.427 – 6.462)	(0.8 – 3.9)	(12 – 59)			
NGC 7213(1)	0.00583900	701410	$6.395^{+0.003}_{-0.008}$	$2.2^{+0.6}_{-0.6}$	$88^{+25}_{-23}$	2.3	0.18	50.9
		/7742/115.3	(6.386 – 6.403)	(1.4 – 3.1)	(57 – 126)			
NGC 7213(2)	0.00583900	701410	$6.412^{+0.016}_{-0.009}$	$2.3^{+1.3}_{-1.1}$	$91^{+50}_{-44}$	2.4	0.18	16.5
		/8590/35.1	(6.395 – 6.431)	(0.9 – 4.2)	(35 – 164)			
NGC 7213(total)	0.00583900	...	$6.395^{+0.008}_{-0.001}$	$2.2^{+0.5}_{-0.6}$	$86^{+22}_{-22}$	2.3	0.18	63.3
		.../150	(6.387 – 6.404)	(1.4 – 3.0)	(56 – 120)			
NGC 7314(1)	0.00474300	700455	$6.397^{+0.015}_{-0.018}$	$1.3^{+1.4}_{-1.1}$	$32^{+34}_{-25}$	3.6	0.18	3.8
		/3016/28.9	...	(0.0 – 3.3)	(0.0 – 81)			
NGC 7314(2)	0.00474300	700455	$6.422^{+0.008}_{-0.009}$	$1.9^{+0.9}_{-0.9}$	$53^{+26}_{-22}$	3.3	0.16	18
		/3719/68.4	(6.387 – 6.437)	(0.8 – 3.2)	(23 – 90)			
NGC 7314(total)	0.00474300	...	$6.413^{+0.017}_{-0.024}$	$1.5^{+0.9}_{-0.8}$	$41^{+24}_{-22}$	3.4	0.17	15.5
		.../95.7	(6.387 – 6.437)	(0.5 – 2.8)	(19 – 76)			
Ark 564	0.0246840	700168	$6.400^f$	$0.6^{+0.4}_{-0.4}$	$25^{+20}_{-16}$	2.7	3.7	2.1
		/863/49.4	...	(0.0 – 1.3)	(0.0 – 58)			
MR 2251-178	0.0639800	700416	$6.412^{+0.008}_{-0.009}$	$0.7^{+0.4}_{-0.4}$	$22^{+12}_{-13}$	2.7	25.3	7.7
		/2977/148.7	(6.396 – 6.427)	(0.1 – 1.3)	(3.0 – 40)			
NGC 7469(1)	0.0163170	700395	$6.388^{+0.007}_{-0.007}$	$2.6^{+0.8}_{-0.7}$	$93^{+30}_{-24}$	2.7	1.6	46.1
		/2956/79.9	(6.380 – 6.396)	(1.6 – 3.8)	(58 – 137)			
NGC 7469(2)	0.0163170	700586	$6.437^{+0.008}_{-0.017}$	$1.6^{+0.8}_{-0.7}$	$60^{+33}_{-25}$	2.4	1.5	16.7
		/3147/69.8	(6.412 – 6.451)	(0.6 – 2.7)	(23 – 104)			
NGC 7469(total)	0.0163170	...	$6.388^{+0.002}_{-0.008}$	$1.9^{+0.6}_{-0.5}$	$72^{+21}_{-20}$	2.6	1.5	50.9
		.../147.2	(6.379 – 6.397)	(1.2 – 2.8)	(44 – 104)			

Note. — Results from *Chandra* HEG data, fitted with a power law plus Gaussian emission-line model in the 2–7 keV band, with the line width fixed at 1 eV. All parameters are quoted in the source rest frame. Statistical errors are for the 68% confidence level, whilst parentheses show the 90% confidence level ranges of the parameters. The number of interesting parameters assumed for calculating the statistical errors was equal to the number of free parameters in the Gaussian component of the model. Col.(1): Redshifts obtained from NASA Extragalactic Database (NED); Col.(2): Observation sequence number, ID, and exposure time in ks; Col.(3): Gaussian line centroid energy; Col.(4): Emission-line intensity in units of  $10^{-5}$  photons  $\text{cm}^{-2}$   $\text{s}^{-1}$ ; Col.(5): Emission line equivalent width; Col.(6):  $F$  is the estimated 2–10 keV observed flux in units of  $10^{-11}$  ergs  $\text{cm}^{-2}$   $\text{s}^{-1}$ . The power-law continuum was extrapolated to 10 keV; Col.(7):  $L$  is the estimated unabsorbed 2–10 keV source-frame luminosity (using the 2–10 keV estimated flux), in units of  $10^{43}$  ergs  $\text{s}^{-1}$ ; Col.(8): The decrease in the fit statistic,  $C$ , when the narrow, two-parameter emission line was added to the continuum-only model.

Table 2. PARAMETERS OF THE CORE FE K LINE EMISSION ( $\sigma$  FREE) FROM *Chandra* (HEG) DATA

Source (1)	$E^a$ (2)	$I^b$ (3)	$EW^c$ (4)	FWHM <sup>d</sup> (Fe K $\alpha$ ) (5)	FWHM <sup>d</sup> (H $\beta$ ) (6)	Reference <sup>e</sup> (7)
Fairall 9	6.370 <sup>+0.347</sup> <sub>-0.161</sub> (6.137 – 6.906)	5.5 <sup>+13.3</sup> <sub>-3.6</sub> (1.5 – 22.9)	228 <sup>+555</sup> <sub>-149</sub> (63 – 954)	18100 <sup>+76840</sup> <sub>-12390</sub> (5100 – 121780)	6270 $\pm$ 290	N06
Mrk 590	6.407 <sup>+0.036</sup> <sub>-0.033</sub> (6.358 – 6.461)	1.6 <sup>+1.0</sup> <sub>-0.8</sub> (0.6 – 3.0)	171 <sup>+103</sup> <sub>-84</sub> (64 – 317)	4350 <sup>+6060</sup> <sub>-2030</sub> (1740 – 15420)	2640	M03
NGC 985	6.407 <sup>+0.070</sup> <sub>-0.076</sub> (6.281 – 6.509)	2.2 <sup>+1.6</sup> <sub>-1.2</sub> (0.6 – 4.4)	170 <sup>+127</sup> <sub>-94</sub> (46 – 344)	9550 <sup>+11190</sup> <sub>-4760</sub> (3810 – 29590)	7500	M03
ESO 198–G24(2)	6.385 <sup>+0.013</sup> <sub>-0.019</sub> (6.353 – 6.404)	1.2 <sup>+0.7</sup> <sub>-0.6</sub> (0.4 – 2.2)	158 <sup>+105</sup> <sub>-80</sub> (57 – 304)	< 4220 (0 – 5840)	6400	Z05
ESO 198–G24(total)	6.382 <sup>+0.025</sup> <sub>-0.043</sub> (6.306 – 6.426)	0.9 <sup>+0.8</sup> <sub>-0.4</sub> (0.3 – 2.1)	117 <sup>+110</sup> <sub>-50</sub> (40 – 279)	2940 <sup>+8830</sup> <sub>-1880</sub> (0 – 15500)	...	...
3C 120	6.410 <sup>+0.016</sup> <sub>-0.015</sub> (6.389 – 6.439)	3.4 <sup>+1.9</sup> <sub>-1.5</sub> (1.4 – 6.0)	66 <sup>+37</sup> <sub>-30</sub> (27 – 117)	2230 <sup>+2280</sup> <sub>-1650</sub> (0 – 5950)	5370	W09
NGC 2110(1)	6.389 <sup>+0.098</sup> <sub>-0.026</sub> (6.341 – 6.521)	6.8 <sup>+10.1</sup> <sub>-3.3</sub> (2.5 – 20.1)	116 <sup>+171</sup> <sub>-56</sub> (43 – 342)	4070 <sup>+15260</sup> <sub>-2470</sub> (0 – 24160)	1200*	M07
NGC 2110(3)	6.394 <sup>+0.009</sup> <sub>-0.007</sub> (6.384 – 6.407)	5.3 <sup>+2.1</sup> <sub>-1.8</sub> (2.9 – 8.2)	87 <sup>+35</sup> <sub>-21</sub> (48 – 135)	< 2540 (0 – 3160)	...	...
NGC 2110(4)	6.395 <sup>+0.010</sup> <sub>-0.010</sub> (6.381 – 6.409)	5.2 <sup>+1.5</sup> <sub>-1.2</sub> (3.3 – 7.6)	127 <sup>+40</sup> <sub>-37</sub> (80 – 184)	2510 <sup>+2070</sup> <sub>-1240</sub> (940 – 5600)	...	...
NGC 2110(total)	6.397 <sup>+0.006</sup> <sub>-0.006</sub> (6.389 – 6.405)	5.3 <sup>+1.0</sup> <sub>-1.2</sub> (3.8 – 6.6)	103 <sup>+21</sup> <sub>-23</sub> (75 – 129)	2320 <sup>+810</sup> <sub>-800</sub> (1320 – 3510)	...	...
PG 0844+349(1)	6.583 <sup>+0.122</sup> <sub>-0.116</sub> (6.422 – 6.770)	2.5 <sup>+1.6</sup> <sub>-1.3</sub> (0.8 – 4.7)	587 <sup>+384</sup> <sub>-303</sub> (189 – 1117)	20320 <sup>+13170</sup> <sub>-8080</sub> (8900 – 44490)	2150	Z05
MCG –5-23-16(1)	6.384 <sup>+0.011</sup> <sub>-0.011</sub> (6.369 – 6.399)	10.6 <sup>+3.2</sup> <sub>-3.1</sub> (6.5 – 15.0)	82 <sup>+25</sup> <sub>-24</sub> (51 – 117)	2630 <sup>+1340</sup> <sub>-880</sub> (1470 – 4560)	1450 <sup>†</sup>	L02
MCG –5-23-16(2)	6.408 <sup>+0.024</sup> <sub>-0.033</sub> (6.359 – 6.452)	8.1 <sup>+5.1</sup> <sub>-4.1</sub> (2.8 – 15.1)	65 <sup>+42</sup> <sub>-33</sub> (23 – 122)	3810 <sup>+4880</sup> <sub>-1690</sub> (1540 – 18350)	...	...
MCG –5-23-16(3)	6.388 <sup>+0.019</sup> <sub>-0.024</sub> (6.352 – 6.416)	9.6 <sup>+4.7</sup> <sub>-4.7</sub> (3.7 – 18.0)	78 <sup>+44</sup> <sub>-38</sub> (30 – 146)	2660 <sup>+4150</sup> <sub>-1580</sub> (610 – 10420)	...	...
MCG –5-23-16(total)	6.388 <sup>+0.009</sup> <sub>-0.009</sub> (6.377 – 6.400)	9.0 <sup>+2.1</sup> <sub>-2.2</sub> (6.1 – 12.1)	71 <sup>+17</sup> <sub>-17</sub> (48 – 96)	2560 <sup>+1130</sup> <sub>-900</sub> (1390 – 4180)	...	...
NGC 3516(1)	6.392 <sup>+0.005</sup> <sub>-0.006</sub> (6.385 – 6.399)	3.9 <sup>+1.2</sup> <sub>-1.3</sub> (2.3 – 5.6)	110 <sup>+34</sup> <sub>-36</sub> (65 – 158)	< 1670 (0 – 3160)	3353 $\pm$ 310	P04
NGC 3516(2)	6.408 <sup>+0.010</sup> <sub>-0.011</sub> (6.393 – 6.422)	4.4 <sup>+2.0</sup> <sub>-1.7</sub> (2.2 – 7.2)	186 <sup>+85</sup> <sub>-71</sub> (93 – 306)	1740 <sup>+1420</sup> <sub>-1210</sub> (0 – 4020)	...	...
NGC 3516(3)	6.402 <sup>+0.017</sup> <sub>-0.014</sub> (6.382 – 6.425)	4.5 <sup>+1.6</sup> <sub>-1.4</sub> (2.7 – 6.7)	157 <sup>+56</sup> <sub>-49</sub> (94 – 234)	4290 <sup>+2180</sup> <sub>-1470</sub> (2450 – 8050)	...	...
NGC 3516(4)	6.409 <sup>+0.023</sup> <sub>-0.025</sub> (6.374 – 6.442)	4.2 <sup>+3.1</sup> <sub>-2.0</sub> (1.6 – 8.3)	67 <sup>+51</sup> <sub>-31</sub> (26 – 134)	3220 <sup>+3020</sup> <sub>-1630</sub> (960 – 8190)	...	...
NGC 3516(5)	6.354 <sup>+0.057</sup> <sub>-0.079</sub> (6.241 – 6.431)	5.1 <sup>+4.1</sup> <sub>-2.6</sub> (1.7 – 10.6)	101 <sup>+81</sup> <sub>-52</sub> (34 – 209)	8480 <sup>+7050</sup> <sub>-4700</sub> (3110 – 18840)	...	...
NGC 3516(6)	6.407 <sup>+0.033</sup> <sub>-0.034</sub> (6.364 – 6.451)	7.6 <sup>+3.7</sup> <sub>-3.4</sub> (3.3 – 12.6)	108 <sup>+52</sup> <sub>-49</sub> (47 – 178)	6030 <sup>+3550</sup> <sub>-2430</sub> (2970 – 11240)	...	...
NGC 3516(7)	6.414 <sup>+0.017</sup> <sub>-0.017</sub> (6.389 – 6.437)	4.2 <sup>+2.4</sup> <sub>-2.0</sub> (1.7 – 7.5)	55 <sup>+32</sup> <sub>-26</sub> (23 – 99)	2290 <sup>+2150</sup> <sub>-1310</sub> (460 – 5900)	...	...
NGC 3516(total)	6.404 <sup>+0.007</sup> <sub>-0.007</sub> (6.395 – 6.413)	4.4 <sup>+0.8</sup> <sub>-0.7</sub> (3.4 – 5.5)	91 <sup>+17</sup> <sub>-14</sub> (71 – 114)	3180 <sup>+880</sup> <sub>-670</sub> (2310 – 4390)	...	...
NGC 3783(1)	6.396 <sup>+0.014</sup> <sub>-0.013</sub> (6.377 – 6.415)	5.4 <sup>+2.7</sup> <sub>-2.6</sub> (2.3 – 9.1)	69 <sup>+36</sup> <sub>-33</sub> (30 – 118)	< 4670 (0 – 5780)	3570 $\pm$ 190	N06
NGC 3783(2)	6.401 <sup>+0.006</sup> <sub>-0.0063</sub> (6.392 – 6.410)	5.1 <sup>+1.5</sup> <sub>-1.1</sub> (3.6 – 7.1)	75 <sup>+21</sup> <sub>-16</sub> (53 – 104)	1930 <sup>+1080</sup> <sub>-900</sub> (750 – 3490)	...	...
NGC 3783(3)	6.391 <sup>+0.008</sup> <sub>-0.008</sub> (6.380 – 6.401)	6.2 <sup>+1.4</sup> <sub>-1.5</sub> (4.3 – 8.2)	90 <sup>+22</sup> <sub>-21</sub> (63 – 120)	2700 <sup>+1180</sup> <sub>-1050</sub> (1410 – 4430)	...	...
NGC 3783(4)	6.395 <sup>+0.005</sup> <sub>-0.006</sub> (6.388 – 6.402)	6.0 <sup>+1.3</sup> <sub>-1.4</sub> (4.2 – 7.8)	88 <sup>+19</sup> <sub>-21</sub> (62 – 114)	1860 <sup>+880</sup> <sub>-1140</sub> (0 – 3140)	...	...
NGC 3783(5)	6.395 <sup>+0.004</sup> <sub>-0.005</sub> (6.388 – 6.401)	6.3 <sup>+1.5</sup> <sub>-1.1</sub> (4.8 – 8.3)	69 <sup>+16</sup> <sub>-12</sub> (53 – 91)	1280 <sup>+720</sup> <sub>-630</sub> (0 – 2260)	...	...
NGC 3783(6)	6.399 <sup>+0.006</sup> <sub>-0.006</sub> (6.391 – 6.408)	4.7 <sup>+1.2</sup> <sub>-1.2</sub> (3.2 – 6.4)	57 <sup>+14</sup> <sub>-15</sub> (39 – 77)	1520 <sup>+890</sup> <sub>-940</sub> (0 – 2750)	...	...
NGC 3783(total)	6.396 <sup>+0.003</sup> <sub>-0.002</sub> (6.393 – 6.399)	5.6 <sup>+0.5</sup> <sub>-0.6</sub> (4.8 – 6.3)	74 <sup>+7</sup> <sub>-8</sub> (63 – 83)	1750 <sup>+360</sup> <sub>-360</sub> (1270 – 2240)	...	...
NGC 4051	6.417 <sup>+0.039</sup> <sub>-0.036</sub> (5.750 – 6.474)	3.5 <sup>+1.4</sup> <sub>-1.4</sub> (1.6 – 5.5)	195 <sup>+79</sup> <sub>-78</sub> (89 – 307)	6430 <sup>+11800</sup> <sub>-2860</sub> (2840 – 479470)	1200	W09
NGC 4151(1)	6.396 <sup>+0.006</sup> <sub>-0.006</sub> (6.386 – 6.404)	21.7 <sup>+3.3</sup> <sub>-4.1</sub> (16.5 – 26.3)	190 <sup>+29</sup> <sub>-36</sub> (146 – 231)	2150 <sup>+1220</sup> <sub>-680</sub> (1250 – 3840)	6350	W09
NGC 4151(2)	6.391 <sup>+0.004</sup> <sub>-0.004</sub> (6.386 – 6.397)	18.2 <sup>+2.7</sup> <sub>-3.5</sub> (14.9 – 21.8)	78 <sup>+11</sup> <sub>-11</sub> (64 – 93)	2170 <sup>+610</sup> <sub>-540</sub> (1460 – 3000)	...	...
NGC 4151(3)	6.396 <sup>+0.006</sup> <sub>-0.005</sub> (6.389 – 6.404)	20.3 <sup>+3.6</sup> <sub>-3.5</sub> (15.7 – 25.3)	83 <sup>+15</sup> <sub>-14</sub> (64 – 103)	2670 <sup>+790</sup> <sub>-680</sub> (1760 – 3770)	...	...

Table 2—Continued

Source (1)	$E^a$ (2)	$I^b$ (3)	$EW^c$ (4)	FWHM <sup>d</sup> (Fe K $\alpha$ ) (5)	FWHM <sup>d</sup> (H $\beta$ ) (6)	Reference <sup>e</sup> (7)
NGC 4151(4)	$6.400^{+0.006}_{-0.005}$ (6.393 – 6.408)	$11.5^{+2.9}_{-2.6}$ (8.1 – 15.5)	$188^{+47}_{-43}$ (132 – 253)	$1710^{+860}_{-740}$ (690 – 2940)	...	...
NGC 4151(5)	$6.393^{+0.016}_{-0.008}$ (6.382 – 6.416)	$14.3^{+8.3}_{-4.2}$ (8.9 – 25.4)	$57^{+33}_{-17}$ (36 – 101)	$2020^{+3600}_{-870}$ (420 – 6750)	...	...
NGC 4151(total)	$6.394^{+0.003}_{-0.002}$ (6.391 – 6.398)	$17.5^{+1.6}_{-1.5}$ (15.5 – 19.7)	$87^{+8}_{-8}$ (77 – 98)	$2250^{+400}_{-360}$ (1770 – 2790)	...	...
3C 273(1)	$6.336^{+0.074}_{-0.053}$ (6.259 – 6.491)	$5.9^{+5.0}_{-4.0}$ (0.6 – 13)	$35^{+29}_{-24}$ (4 – 76)	$5900^{+8640}_{-5830}$ (0 – 80630)	3520	Z05
NGC 4593	$6.406^{+0.011}_{-0.042}$ (6.351 – 6.421)	$3.8^{+3.4}_{-1.4}$ (2.0 – 8.5)	$82^{+74}_{-30}$ (43 – 185)	$2230^{+8180}_{-1100}$ (670 – 15320)	3650	W09
MCG –6-30-15(1)	$6.399^{+0.043}_{-0.045}$ (6.335 – 6.461)	$3.4^{+1.4}_{-1.8}$ (1.0 – 6.1)	$70^{+31}_{-37}$ (21 – 125)	$7440^{+5710}_{-4630}$ (2480 – 16270)	$1700 \pm 170$	N06
MCG –6-30-15(2)	$6.395^{+0.061}_{-0.044}$ (6.298 – 6.485)	$1.9^{+1.4}_{-0.9}$ (0.7 – 3.9)	$40^{+30}_{-19}$ (15 – 83)	$2810^{+15450}_{-1750}$ (0 – 23770)	...	...
MCG –6-30-15(3)	$6.424^{+0.094}_{-0.110}$ (6.237 – 6.557)	$2.8^{+2.1}_{-1.5}$ (0.8 – 5.7)	$62^{+45}_{-34}$ (17 – 124)	$13590^{+12820}_{-6050}$ (5760 – 37720)	...	...
MCG –6-30-15(4)	$6.402^{+0.154}_{-0.023}$ (6.364 – 6.602)	$1.0^{+1.0}_{-0.7}$ (0.1 – 2.3)	$20^{+20}_{-14}$ (2 – 45)	< 14800 (0 – 28590)	...	...
MCG –6-30-15(5)	$6.345^{+0.027}_{-0.024}$ (6.292 – 6.393)	$2.2^{+2.3}_{-1.4}$ (0.3 – 5.3)	$46^{+48}_{-29}$ (6 – 111)	< 5850 (0 – 15200)	...	...
MCG –6-30-15(total)	$6.427^{+0.044}_{-0.044}$ (6.366 – 6.486)	$2.7^{+1.4}_{-0.9}$ (1.5 – 4.1)	$58^{+23}_{-20}$ (32 – 88)	$11880^{+4650}_{-4030}$ (6480 – 18750)	...	...
IRAS 13349+2438(2)	$6.396^{+0.046}_{-0.057}$ (6.306 – 6.486)	$0.7^{+0.5}_{-0.4}$ (0.2 – 1.5)	$170^{+139}_{-93}$ (52 – 386)	$5870^{+11370}_{-2550}$ (2660 – 85550)	...	...
IRAS 13349+2438(total)	$6.405^{+0.052}_{-0.113}$ (6.106 – 6.841)	$0.4^{+0.5}_{-0.2}$ (0.07 – 2.3)	$87^{+121}_{-41}$ (16 – 532)	$5150^{+60200}_{-2810}$ (1770 – 93230)	...	...
IC 4329A	$6.305^{+0.139}_{-0.096}$ (6.172 – 6.542)	$15.8^{+10.6}_{-7.5}$ (5.9 – 31.5)	$81^{+54}_{-38}$ (30 – 162)	$18830^{+18590}_{-9620}$ (5820 – 48080)	$5620 \pm 200$	N06
Mrk 279	$6.414^{+0.054}_{-0.028}$ (6.312 – 6.560)	$2.0^{+1.2}_{-0.9}$ (0.9 – 6.9)	$132^{+80}_{-59}$ (60 – 458)	$5080^{+8390}_{-1940}$ (2670 – 48780)	5150	W09
NGC 5506	$6.400^{+0.007}_{-0.006}$ (6.391 – 6.409)	$7.1^{+1.6}_{-2.1}$ (4.4 – 9.3)	$84^{+18}_{-25}$ (52 – 109)	$1650^{+880}_{-870}$ (470 – 2940)	1850	Z05
NGC 5548(1)	$6.398^{+0.022}_{-0.021}$ (6.367 – 6.427)	$3.7^{+1.5}_{-1.4}$ (1.9 – 5.8)	$124^{+51}_{-46}$ (64 – 195)	$4410^{+2590}_{-1580}$ (2390 – 8500)	$5830 \pm 230$	N06
NGC 5548(2)	$6.402^{+0.009}_{-0.009}$ (6.389 – 6.415)	$2.4^{+0.9}_{-0.7}$ (1.4 – 3.6)	$71^{+27}_{-21}$ (42 – 107)	$1960^{+1040}_{-900}$ (800 – 3540)	...	...
NGC 5548(total)	$6.403^{+0.009}_{-0.009}$ (6.391 – 6.415)	$2.7^{+0.8}_{-0.7}$ (1.8 – 3.7)	$84^{+25}_{-22}$ (56 – 115)	$2540^{+1140}_{-820}$ (1490 – 4240)	...	...
Mrk 290(total)	$6.404^{+0.037}_{-0.038}$ (6.342 – 6.458)	$1.0^{+0.6}_{-0.5}$ (0.2 – 1.9)	$60^{+33}_{-31}$ (12 – 110)	$5290^{+5120}_{-2420}$ (2140 – 20200)	4740	W09
E1821+643	$6.447^{+0.051}_{-0.054}$ (6.355 – 6.517)	$3.2^{+1.6}_{-1.3}$ (1.6 – 5.4)	$153^{+75}_{-63}$ (76 – 257)	$10920^{+7710}_{-3910}$ (5640 – 25950)	$6620 \pm 720$	N06
3C 382(2)	$6.424^{+0.064}_{-0.090}$ (6.254 – 6.531)	$3.6^{+3.2}_{-2.3}$ (0.7 – 8.1)	$66^{+55}_{-43}$ (13 – 144)	$8100^{+12580}_{-4490}$ (3150 – 33320)	8340	W09
3C 382(total)	$6.418^{+0.084}_{-0.097}$ (6.161 – 6.538)	$3.4^{+2.3}_{-2.5}$ (0.4 – 7.1)	$57^{+39}_{-42}$ (7 – 119)	$10730^{+15810}_{-8320}$ (2060 – 55310)	...	...
4C +74.26(total)	$6.260^{+0.038}_{-0.081}$ (6.125 – 6.392)	$1.2^{+2.0}_{-0.8}$ (0.1 – 4.1)	$36^{+60}_{-24}$ (3 – 124)	< 10980 (0 – 23620)	9420	W09
Mrk 509	$6.428^{+0.020}_{-0.021}$ (6.396 – 6.455)	$3.6^{+2.0}_{-1.7}$ (1.4 – 6.4)	$57^{+30}_{-27}$ (22 – 100)	$2910^{+2590}_{-1250}$ (1280 – 7900)	$3430 \pm 240$	N06
NGC 7213(1)	$6.392^{+0.013}_{-0.011}$ (6.377 – 6.410)	$2.9^{+1.7}_{-1.0}$ (1.6 – 4.4)	$117^{+45}_{-40}$ (65 – 179)	$2290^{+1950}_{-1390}$ (390 – 5000)	3200	Z05
NGC 7213(2)	$6.410^{+0.018}_{-0.018}$ (6.384 – 6.436)	$3.2^{+2.0}_{-1.6}$ (1.2 – 6.0)	$126^{+78}_{-63}$ (47 – 236)	$2400^{+2310}_{-1800}$ (0 – 6770)	...	...
NGC 7213(total)	$6.397^{+0.011}_{-0.010}$ (6.384 – 6.412)	$3.0^{+1.0}_{-0.9}$ (1.8 – 4.3)	$120^{+42}_{-35}$ (73 – 174)	$2590^{+1470}_{-1170}$ (1050 – 4620)	...	...
NGC 7469(1)	$6.385^{+0.010}_{-0.012}$ (6.364 – 6.399)	$3.2^{+1.1}_{-1.2}$ (1.7 – 5.1)	$116^{+42}_{-42}$ (63 – 187)	$1800^{+2640}_{-1360}$ (0 – 6040)	2820	W09
NGC 7469(2)	$6.395^{+0.036}_{-0.033}$ (6.347 – 6.452)	$3.9^{+2.0}_{-1.6}$ (1.8 – 6.6)	$156^{+79}_{-64}$ (72 – 262)	$6780^{+4810}_{-3170}$ (3200 – 14100)	...	...
NGC 7469(total)	$6.388^{+0.018}_{-0.017}$ (6.365 – 6.413)	$3.7^{+1.6}_{-1.1}$ (2.2 – 5.2)	$142^{+54}_{-42}$ (84 – 199)	$4890^{+2770}_{-1700}$ (2740 – 8740)	...	...

Note. — Results from *Chandra* HEG data, fitted with a power law plus Gaussian emission-line model in the 2–7 keV band. Statistical errors are for the 68% confidence level, whilst parentheses show the 90% confidence level ranges of the parameters. \* Broad polarized H $\beta$  line. † Infra-red broad Br $\alpha$  line. <sup>a</sup> Gaussian line center energy in keV. <sup>b</sup> Emission-line intensity in units of  $10^{-5}$  photons cm<sup>-2</sup> s<sup>-1</sup>. <sup>c</sup> Emission line equivalent width in units of eV. <sup>d</sup> Full width half maximum, rounded to 10 km s<sup>-1</sup>. <sup>e</sup> References for H $\beta$  FWHM: L02—Lutz et al. (2002); M03—Marziani et al. (2003); M07—Moran et al. (2007); N06—Nandra (2006); P04—Peterson et al. (2004); W09—Wang et al. (2009); Z05—Zhou et al. (2005).

Table 3. MEAN FE K $\alpha$  LINE SPECTRAL PARAMETERS

Parameter	By Observation	# Spectra <sup>a</sup>	By Source	# Sources <sup>b</sup>
Centroid Energy (keV) ( $\sigma_{\text{Fe K}}$ fixed)	$6.396 \pm 0.0004$ <sup>c</sup>	68	$6.397 \pm 0.0005$ <sup>c</sup>	32
Centroid Energy (keV) ( $\sigma_{\text{Fe K}}$ free) <sup>d</sup>	$6.388 \pm 0.001$	68	$6.398 \pm 0.002$	32
EW (eV) ( $\sigma_{\text{Fe K}}$ fixed)	$42 \pm 2$	70	$44 \pm 2$	33
EW (eV) ( $\sigma_{\text{Fe K}}$ free) <sup>d</sup>	$53 \pm 3$	70	$70 \pm 4$	33
FWHM (km s <sup>-1</sup> )	$2060 \pm 230$	53	$2200 \pm 220$	27

Note. — Weighted mean quantities from spectral fitting to individual spectra (“by observation”), and to spectra representative of each source (“by source”). See text, §4 for details. <sup>a</sup> Number of spectra (one per observation) contributing to the mean quantities. <sup>b</sup> Number of unique sources contributing to the mean quantities. <sup>c</sup> These statistical errors are smaller than the systematic errors (see §4.1 for discussion). <sup>d</sup> The intrinsic width of the Fe K $\alpha$  in these cases was free in the spectral fitting for 51 spectra in the individual observation fits (see Table 2) and for 27 sources in the fits to source-representative spectra (see §4 for details).

Table 4. X-RAY BALDWIN EFFECT: FE  $K\alpha$  LINE EW VERSUS LUMINOSITY FITS

Parameter	By Observation	By Source
$\log EW = k_L + [m_L \log(L_x)]$		
$\chi^2$ (d.o.f.)	58.5(68)	24.7(31)
intercept, $k_L$	$1.80^{+0.02}_{-0.02}$	$1.76^{+0.02}_{-0.02}$
slope, $m_L$ (68% confidence errors)	$-0.22^{+0.03}_{-0.03}$	$-0.13^{+0.04}_{-0.04}$
slope, $m_L$ (99% confidence errors)	$-0.22^{+0.10}_{-0.07}$	$-0.13^{+0.11}_{-0.11}$
$\Delta\chi^2$ for $m_L = 0$	39.3	10.0
Significance for $m_L \neq 0$	$6.27\sigma$	$3.24\sigma$
$\log EW = k_R + [m_R \log(L_x/L_{\text{EDD}})]$		
$\chi^2$ (d.o.f.)	61.4 (68)	25.2(31)
intercept, $k_R$ (68% confidence errors)	$1.31^{+0.09}_{-0.09}$	$1.50^{+0.09}_{-0.09}$
slope, $m_R$ (68% confidence errors)	$-0.20^{+0.03}_{-0.03}$	$-0.11^{+0.04}_{-0.04}$
slope, $m_R$ (99% confidence errors)	$-0.20^{+0.07}_{-0.11}$	$-0.11^{+0.09}_{-0.09}$
$\Delta\chi^2$ for $m_R = 0$	36.6	9.5
Significance for $m_R \neq 0$	$6.05\sigma$	$3.08\sigma$

Note. — Results of fitting the relations between the derived Fe  $K\alpha$  line EWs and the 2–10 keV X-ray luminosity ( $L_x$ ), and between the EWs and the Eddington ratio ( $L_x/L_{\text{EDD}}$ ). Coefficients and their error bounds are shown for linear fits to  $\log EW$  versus  $\log(L_x)$  ( $k_L$ ,  $m_L$ ), and to  $\log EW$  versus  $\log(L_x/L_{\text{EDD}})$  for spectral fitting results to the individual spectra (“by observation”), and to the source-representative spectra. See §5 for details. The number of degrees of freedom for each fit (d.o.f.) is shown in parentheses after each best-fitting  $\chi^2$  value.